Influence of planetary rotation on metal-silicate mixing and equilibration in a magma ocean

Quentin Kriaa, Maylis Landeau, Michael Le Bars

Influence of planetary rotation on metal-silicate mixing and equilibration in a magma ocean

Quentin Kriaa* and Michael Le Bars†

Aix Marseille Univ, CNRS, Centrale Marseille, IRPHE, Marseille, France

Maylis Landeau‡

Université de Paris, Institut de Physique du Globe de Paris, CNRS, 75005 Paris, France

(Dated: October 30, 2024)

At a late stage of its accretion, the Earth experienced high-energy planetary impacts. Following each collision, the metal core of the impactor sank into molten silicate magma oceans. The efficiency of chemical equilibration between these silicates and the metal core controlled the composition of the Earth interior and left a signature on geochemical and isotopic data. These data constrain the timing, pressure and temperature of Earth formation, but their interpretation strongly depends on the efficiency of metal-silicate mixing and equilibration. We investigate the role of planetary rotation on the dynamics of the sinking metal and on its chemical equilibration using laboratory experiments of particle clouds settling in a rotating fluid. Our clouds initially sink as spherical turbulent thermals, but after a critical depth, rotation becomes important and they transition to a vortical columnar flow aligned with the rotation axis. Applied to Earth formation, our results predict that rotation strongly affects the fall of metal in the magma ocean for impactors smaller than 459 km in radius on a proto-Earth that rotates twice faster than today. On a proto-Earth spinning 5 times faster than today, rotation is important for any impactor smaller than the Earth itself. In contrast with a thermal that grows in all directions, the vortical column grows vertically but keeps a constant horizontal extent. The slower dilution in vortical columns reduces chemical equilibration compared to previous estimates that neglect planetary rotation. We find that rotation significantly affects the degree of equilibration for highly siderophile elements with partition coefficients larger than 10^3. In this case, for a planet spinning twice faster than today, the degree of equilibration decreases by up to a factor 2 compared to previous estimates that neglect the effect of rotation. Finally, the ultimate fate of iron drops is to be detrained from the vortical column as an iron rain, reconciling the traditional iron rain scenario with the model of turbulent thermal.

Key words: Planetary impacts, planetary rotation, metal-silicate mixing, turbulent thermal, composition and structure of the planets

I. INTRODUCTION

The present-day terrestrial planets of the solar system were formed 4.5 Gyrs ago (Patterson et al. 1955) by a series of impacts between planetary bodies. Moon-to-Mars-sized planetary embryos collided to form planets in $10-100$ Myrs (Chambers 2004). This timing is confirmed by Hf-W radiochronometry which suggests that the Earth and the Moon were formed within the first 100 Myrs (Kleine et al. 2002, Rudge et al. 2010) of the solar system. At this time, planetary embryos were already differentiated into a liquid metal core and an outer silicate mantle (Kleine et al. 2002). During impacts, some of the metal core of impactors was mixed with silicates of the target planet, enabling thermal and chemical transfers. This mixing controlled the initial temperature and composition of rocky planets which determined the initial rheology of the mantle and the emergence of plate tectonics (Bercovici and Ricard 2014), the time when a solid inner core started to grow (Labrosse 2015), or the driving of an early dynamo in the Earth's core by exsolution of light elements (Badro et al. 2018).

Accretion of rocky planets goes through several successive stages involving ever larger impactors. The size of impactors varies from small kilometre-sized planetesimals to embryos as large as Mars or the Earth (Canup 2012, Canup and Asphaug 2001, Ćuk and Stewart 2012, Tonks and Melosh 1993). When the target embryo is the size of Mars or larger, the energy released during the impact is sufficient for shock waves to melt the silicate mantle much beyond the impact area (Nakajima et al. 2021, Tonks and Melosh 1992). Previous studies (Nakajima et al. 2021, Tonks and Melosh 1993) showed that a Mars-sized impactor hitting the Earth at a velocity larger than 11 km/s produces enough melt to uniformly cover the Earth surface down to a depth of 1000 km or more. The smaller the impactor or the target, the lower the volume of molten silicates produced by the shock in the target planet (Tonks and Melosh 1992, 1993). Yet a series of small impactors may release sufficient energy to melt silicates at large depths, especially if the target surface is blanketed by a steam atmosphere (Abe and Matsui 1985) reducing heat losses to space. Finally, during the first million years of accretion, radioactive elements like ^{26}Al (Dodds et al. 2021) released enough energy to melt the entire mantle of the target planet. In the following, we consider that any combination of the former ingredients enables the existence of a deep magma ocean, in which the impactor core sinks after an impact.

* Corresponding author: quentin.kriaa@univ-amu.fr
† michael.le-bars@univ-amu.fr
‡ landeau@ipgp.fr

The fall of the impactor core in the magma ocean is strongly conditioned by the outcome of the impact. Numerical simulations are valuable tools to investigate the dynamics of impacts with various impactor sizes, impact angles or impact velocities (e.g., Ćuk and Stewart 2012, Maas et al. 2021, Nakajima et al. 2021). Yet, evaluating chemical transfers requires to resolve mixing and diffusive processes at the metal-silicate interface. The length scale for chemical diffusion during the fall of metal in a magma ocean, which typically lasts a few hours, is on the order of 1 cm (Dahl and Stevenson 2010). Unfortunately, numerical simulations are only able to resolve length scales which are several orders of magnitude larger than this diffusive length scale (Dahl and Stevenson 2010). Landeau et al. (2021) and Lherm et al. (2022) recently investigated the phase of mixing by impacts using laboratory experiments with miscible fluids, approaching dynamical regimes of planetary collisions. These experiments evidenced substantial mixing down to small scales during the impact stage, increasing the volume of silicates mixed and equilibrated with the impactor metal. They also suggested that much of the impactor kinetic energy is imparted to the silicates during impact, so that metal from the impactor starts sinking with negligible velocity (see Fig. 3 and Fig. 7a in Landeau et al. 2021).

One of the key parameters controlling chemical transfers is the surface area of the metal-silicate interface per unit mass of metal. Past studies have investigated metal-silicate mixing through mainly two modelling approaches. The first approach considered that, after impact, the impactor core quickly emulsified into millimetre-to-centimetre-sized spherical drops, which settle downward. This so-called *iron rain* model (Rubie et al. 2003) has been refined by several analytical and numerical studies, which incorporated subtle aspects of the drops dynamics and diffusive transfers (Ichikawa et al. 2010, Maas et al. 2021, Qaddah et al. 2019, Ulvrová et al. 2011).

While emulsification during impact remains to be investigated, fluid mechanics experiments showed that breakup happens after a descent of a few initial radii of the sinking core (Landeau et al. 2014, Wacheul and Le Bars 2018). These experiments showed that drops do not settle individually as an iron rain. Instead they favoured a second modelling approach. As the impactor core falls in the magma ocean, it forms a turbulent cloud that entrains silicates at a rate proportional to the cloud surface area and downward velocity, with a proportionality constant $\alpha = 0.25 \pm 0.10$ called the coefficient of entrainment (Morton et al. 1956). This entrainment dilutes the metal within the cloud, which therefore decelerates while its radius r increases linearly in depth z at a rate $dr/dz = \alpha$. In this model the cloud is called a turbulent thermal; it accurately accounts for stirring between miscible (Deguen et al. 2014, Landeau et al. 2021, Morton et al. 1956), immiscible (Landeau et al. 2014, Lherm and Deguen 2018, Wacheul and Le Bars 2018) and particle-laden fluids (Deguen et al. 2011, Kriaa et al. 2022). Thus, this model predicts stirring before and after the core breaks up into droplets (Deguen et al. 2014, Wacheul and Le Bars 2018). A major consequence for chemical

transfers is that metal equilibrates only with the finite volume of silicates that is entrained in the cloud. Yet, these previous studies have ignored the effect of planetary rotation on metal-silicate equilibration (Dahl and Stevenson 2010), despite the strong rotation rate of the proto-Earth that has been suggested by impact simulations (Ćuk and Stewart 2012).

This neglect likely originates from considering the earliest models for metal-silicate mixing. In the iron-rain scenario (Ichikawa et al. 2010, Qaddah et al. 2019, Rubie et al. 2003, Ulvrová et al. 2011) metal drops of ~ 1 cm in radius fall in the magma ocean at a velocity of $\sim 0.2 - 0.5$ m/s, meaning that they settle in 10 to 100 days at the bottom of a 1000 km-deep magma ocean. Although this timescale is much longer than the length of day, the size of such drops is too small for planetary rotation to influence their dynamics. The strength of rotation is quantified by the ratio of inertial forces over the Coriolis force, the so-called Rossby number, which is on the order of 10^5 for an individual drop. This high value suggests that rotation is negligible at the scale of a drop. To estimate the effect of rotation at larger length scales, one can assume that an entire impactor core of 100 to 1000 km in radius falls as a whole under the buoyancy force. The resulting sinking velocity is on the order of 1 km/s, meaning that the impactor core reaches the bottom of the ocean in about one hour (Dahl and Stevenson 2010). This fall time is now too short compared to the length of day for rotation to be important. The corresponding Rossby number is indeed larger than 10. However, this latter estimate entirely neglects the formation of a turbulent cloud of metal and silicates. Previous fluid mechanics experiments have found that the large-scale flow in a thermal or a particle-laden cloud is easily affected by rotation (Ayotte and Fernando 1994, Bush 2003, Helfrich 1994, Kriaa et al. 2022, Lai et al. 2016, Rahimipour and Wilkinson 1992). In the present study, we show that planetary rotation affects the fall of metal-silicate clouds in magma oceans because the clouds grow with depth by turbulent entrainment and they also decelerate, which enhances the magnitude of the Coriolis force relative to inertial forces.

The influence of planetary rotation on the fate of the impactor core has recently been investigated with numerical simulations by Maas et al. (2021) for a few scenarios of impacts on Earth in a global magma ocean. These simulations showed that planetary rotation, and the latitude of the impact point, affect the dispersion and settling of iron drops in the magma ocean. However, because of the high numerical cost, the smallest drop size is 100 m in these simulations. In addition, the authors do not quantify the effect of rotation on the turbulent mixing in a metal-silicate cloud.

In the present study we focus on the scenario of an impact at the pole, with gravity and rotation aligned, and we model the post-impact flow using our recent laboratory experiments of rotating particle clouds (Kriaa et al. 2022). We quantify the role of planetary rotation varying the angular velocity and gravity of the target planet, the drop size

and the impactor size.

Section II introduces the experimental framework that models the post-impact flow using particle-laden clouds settling in a water tank in solid body rotation. In particular, section II C summarises the key features of the dynamical regimes of these clouds on the basis of the results presented in Kriaa et al. (2022). We show that clouds initially behave as turbulent thermals, but transform into vortical columns aligned with the axis of rotation when the thermal's Rossby number becomes lower than unity. This columnar flow is modelled in section III. Its consequences on the dilution of metal, and its implications on the efficiency of chemical transfers between metal and silicates are presented in section IV. We discuss the limitations of our work and we suggest ideas for future investigations in section V.

II. EXPERIMENTAL MODELLING

A. Experimental setup

We briefly introduce the experimental setup, which is presented with more details in Kriaa et al. (2022). The apparatus is illustrated in figure 1. The experiments are performed in a Plexiglas tank of height 90 cm and cross-section area 42×42 cm^2 containing 160 L of fresh water ($\rho_f = 998$ kg.m^{-3}, $\nu = 10^{-6}$ m^2.s^{-1}). The tank is fixed in the middle of a rotating table whose angular velocity Ω varies from 0 (no rotation) to 20 rotations per minute (rpm). A lid is placed on top of the tank with a hole at the centre. Placed in this hole, a cylinder of inner diameter $D_{\text{cyl}} = 3.2$ cm contains the buoyant material. The cylinder's bottom nozzle is sealed by a latex membrane, which is stretched and taped onto the cylinder. We then pour the buoyant material into the cylinder.

The released fluid is either made of salt water, which stands as a particle-free reference, or it is composed of a mixture of 26.1 mL of fresh water and a fixed mass $m_0 = 1.0$ g of spherical glass beads of density $\rho_p = 2500$ kg.m^{-3}. The mean radius r_p of the beads ranges from 2.6 μm to 524.5 μm (see table I). In all the experiments the total mass excess introduced into the system is the same. In this setup, the ambient water in the tank is an analogue for the silicate magma ocean and the released particles are analogues for the drops of liquid metal, as previously proposed by Deguen et al. (2011).

The ambient water and the tank are either both motionless or in solid-body rotation. At $t = 0$ the experiment starts by rupturing the latex membrane with a needle, releasing the content of the cylinder. Once the membrane retracts, the particles fall out of the cylinder because of their weight. For most particle sizes, the downward acceleration of the particles quickly transmits to the fluid, the buoyant material rolls up and the cloud becomes turbulent after a

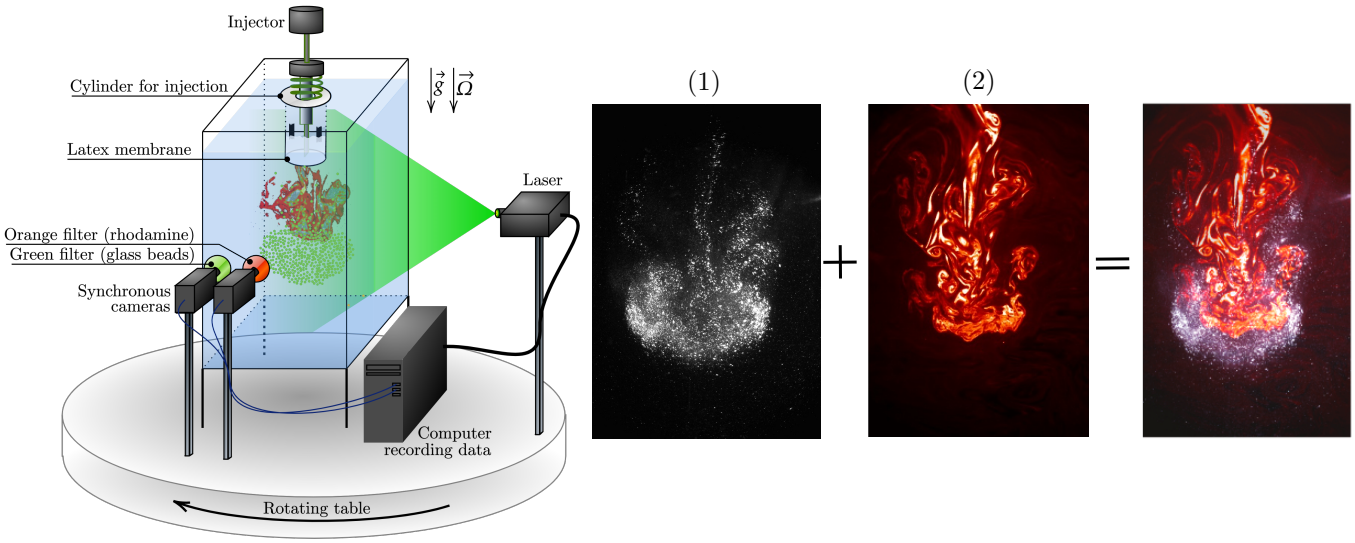

FIG. 1: Schematic representation of the experimental apparatus, and examples of images of (1) the glass beads using a green filter and (2) the released water volume using an orange filter.

distance of about $1D_{\rm cyl}$.

The typical cloud velocity at a depth $\sim D_{\rm cyl}$ reads

$$U_{\rm ref} = \sqrt{g\left(1-\frac{\rho_f}{\rho_0}\right)D_{\rm cyl}}, \tag{1}$$

with $g = 9.81$ m.s^{-2} and ρ_0 the initial cloud density once it has rolled up as a sphere of typical radius $D_{\rm cyl}$, hence

$$\rho_0 = \rho_f + \left(1-\frac{\rho_f}{\rho_p}\right)\frac{3m_0}{4\pi D_{\rm cyl}^3}. \tag{2}$$

Note that the values of ρ_0 and $U_{\rm ref}$ are respectively fixed to 1002.4 kg/m^3 and 3.7 cm/s for all experiments.

Visualisations are performed in a vertical laser sheet (532 nm). Since particles and water have different motions, two identical black-and-white cameras are synchronised and record at 50 fps the same experiment with two different filters. The first camera has a green filter to record the motion of glass beads, which reflect and refract the laser beam, while the second camera has an orange filter. By colouring the fluid inside the cylinder with a fluorescent dye called rhodamine, the second camera records the motion of the released water volume which appears in orange in the laser sheet. Both of them record the same field of view of size 45 cm $\times$ 28 cm.

B. Governing dimensionless numbers

Assuming the tank is large enough to neglect its influence on the clouds' dynamics, the motion of particles depends on gravity g, the ambient fluid density ρ_f and kinematic viscosity ν_f, the particles' density ρ_p, the total mass of particles in a cloud m_0, the diameter of the cylinder $D_{\rm cyl}$, the average radius of particles r_p (we neglect the polydispersity of clouds and refer the reader to Kriaa et al. (2022) for more details), and finally the tank angular velocity Ω.

The motion of particles is characterised by their settling velocity w_s. To compute w_s we use in this study the model proposed by Samuel (2012)

$$w_s = \frac{20\nu_f}{r_p}\left[\sqrt{1+\frac{(\rho_p-\rho_f)gr_p^3}{45\rho_f\nu_f^2}}-1\right]. \tag{3}$$

According to the Vaschy-Buckingham theorem, five independent dimensionless numbers can be computed from the eight dimensional quantities (g, ρ_f, ρ_p, ν_f, m_0, $D_{\rm cyl}$, r_p and Ω) that govern the particles' motion. Three numbers that we kept constant in experiments are the density ratio ρ_p/ρ_f, the initial volume fraction of particles, which reads $\phi_0 = 3m_0/4\pi\rho_p D_{\rm cyl}^3$ for a cloud of typical radius $D_{\rm cyl}$, and the initial cloud Reynolds number

$$Re_{\rm cloud} = \frac{2D_{\rm cyl}U_{\rm ref}}{\nu_f} \tag{4}$$

which quantifies the predominance of inertial forces over viscous forces at early times. We varied the Rouse number

$$\mathcal{R} = \frac{w_s}{U_{\rm ref}} \tag{5}$$

that characterises the motion of particles. Usually used for sediment transport (de Leeuw et al. 2020) and previously used to study metal-silicates mixing in experiments (Deguen et al. 2011), the Rouse number compares the settling speed of a particle w_s and that of the cloud $U_{\rm ref}$. Since the reference fluid velocity $U_{\rm ref}$ is the same for all experiments (equation (1)), the Rouse number only varies with the particles' radius: the larger the particle, the larger the Rouse number. As particles get smaller and smaller, their Rouse number goes to 0 so their gravitational drift due to settling vanishes, hence they behave more and more as salt water, which corresponds to the asymptote $\mathcal{R} = 0$. Conversely when their Rouse number is larger than unity, the settling speed of particles is so large that the motions of water and particles are decoupled. Our experiments explore the transition between these end members.

Finally, the initial cloud Rossby number

$$Ro_{\text{cloud}} = \frac{U_{\text{ref}}}{2\Omega D_{\text{cyl}}} \tag{6}$$

quantifies the balance between inertia and the Coriolis force at early times: the larger this number, the more inertial the cloud is initially.

Reference values of the five governing numbers can be found in table I for both the experiments and for clouds of liquid iron drops falling in molten silicates. We also give values of the particle Reynolds number Re_p that is commonly used to determine the dynamical regime of the flow going past the settling particles. From table I, we note that the density ratio, the Rouse numbers and the particle Reynolds numbers that we investigate match with the values expected in planetary flows. Particles are in the dilute regime in both cases ($\phi \ll 1$) and the particle clouds are in the turbulent regime ($Re_{\text{cloud}} \gg 1$). Finally, our values of cloud Rossby number also match with the values expected for planetary flows.

The appropriate number that quantifies the influence of background rotation throughout the cloud fall is the depth-dependent Rossby number

$$Ro(z) = \frac{\dot{z}_f(z)}{2\Omega r(z)}, \tag{7}$$

where $\dot{z}_f(z)$ is the vertical velocity of the front of a spherical particle cloud with radius $r(z)$ at depth z. The front velocity $\dot{z}_f$ is used rather than the velocity of the centre of mass, because the front is easy to track from videos and more meaningful due to the large detrainment of particles happening at large times – see the next sections and Kriaa et al. (2022) for details. The Rossby number is the ratio of the cloud inertia over the Coriolis force. In experiments $Ro(z \leq D_{\text{cyl}}) > 1$, so that particle clouds are initially weakly influenced by rotation. However, the Rossby number decreases as the cloud falls, and rotation starts affecting the dynamics when the Rossby number equals unity.

C. Dynamical regimes in particle-cloud experiments

Our experiments (Kriaa et al. 2022) showed that, as the particle cloud sinks, it transitions from a regime of turbulent thermal, in which rotation is negligible, to a regime of vortical column that is strongly influenced by rotation. This section recalls the essential features of the regimes relevant for the planetary application, namely the turbulent thermal

Quantity	Experiments	Planetary flows
r_p	$2.6 - 525$ μm	1000 μm
Cloud size	$D_{\rm cyl} = 0.032$ m	$R = 1$ km $- R_\oplus/3$
ρ_p/ρ_f	2.5	2.23
$\mathcal{R}$	$7.6 \times 10^{-2} - 4.13$	$1.4 \times 10^{-4} - 1.2 \times 10^{-1}$
Re_p	$1.2 \times 10^{-4} - 160$	20.8
ϕ_0	2.9×10^{-3}	$3.1 \times 10^{-5} - 2.1 \times 10^{-1}$
$Re_{\rm cloud}$	$2.4 \times 10^3 \gg 1$	$3.1 \times 10^9 - 3.0 \times 10^{14}$
$Ro_{\rm cloud}$	$0.28 - 1.1$	$0.25 - 1.9$

TABLE I: Comparison of the governing dynamical numbers for experiments and clouds of liquid iron drops falling in molten silicates. We assume an impactor hitting the Earth with $g = 9.81$ m.s^{-2} and the Earth rotation rate being twice larger than today, which is the most common scenario we consider in this study. Note that experimental values are based on the results published in Kriaa et al. (2022) where the settling velocity is calculated from the classic Schiller-Naumann equation. In the present study we use equation (3) due to its wider range of applicability. The cloud Reynolds number is computed with the kinematic viscosity of the ambient fluid (water in experiments and silicates in magma oceans, see table II); both $Re_{\rm cloud}$ and $Ro_{\rm cloud}$ are based on the reference velocity of equation (1), and their reference length scale is respectively $D_{\rm cyl}$ in experiments, and the post-impact cloud radius r_0 for planetary flows (see section IV and equation 15 in Landeau et al. (2021)).

and vortical column regimes. In experiments, we also observe a third regime, called *swarm*. For completeness, it is briefly described in appendix A but not detailed in the main text as this regime is unlikely after planetary impacts (see e.g. Deguen et al. 2011).

1. *Regime of turbulent thermal*

In our experiments, particle clouds start their motion in the same way as salt water clouds: they form a so-called thermal, which is a finite volume of buoyant fluid whose motion is entirely governed by its total buoyancy. Our thermals quickly become turbulent during a short phase of acceleration at depths $\lesssim D_{\rm cyl}$. Subsequently, turbulence entrains ambient fluid into the clouds and hence leads to their growth with depth. Because of this progressive entrainment and dilution, the clouds eventually decelerate. Entrainment can be modelled by assuming that the inflow velocity v_e of ambient fluid entrained into the thermal is proportional to the vertical velocity $\dot{z}$ of the turbulent thermal (Morton et al. 1956). In a uniform ambient fluid, this model predicts that the cloud radius r is proportional to the cloud depth z so that $r = r_0 + \alpha z$, with r_0 the initial cloud radius and $\alpha = 0.25 \pm 0.1$ the entrainment coefficient (Deguen et al. 2011, Landeau et al. 2014).

2. *Transition to vortical columns*

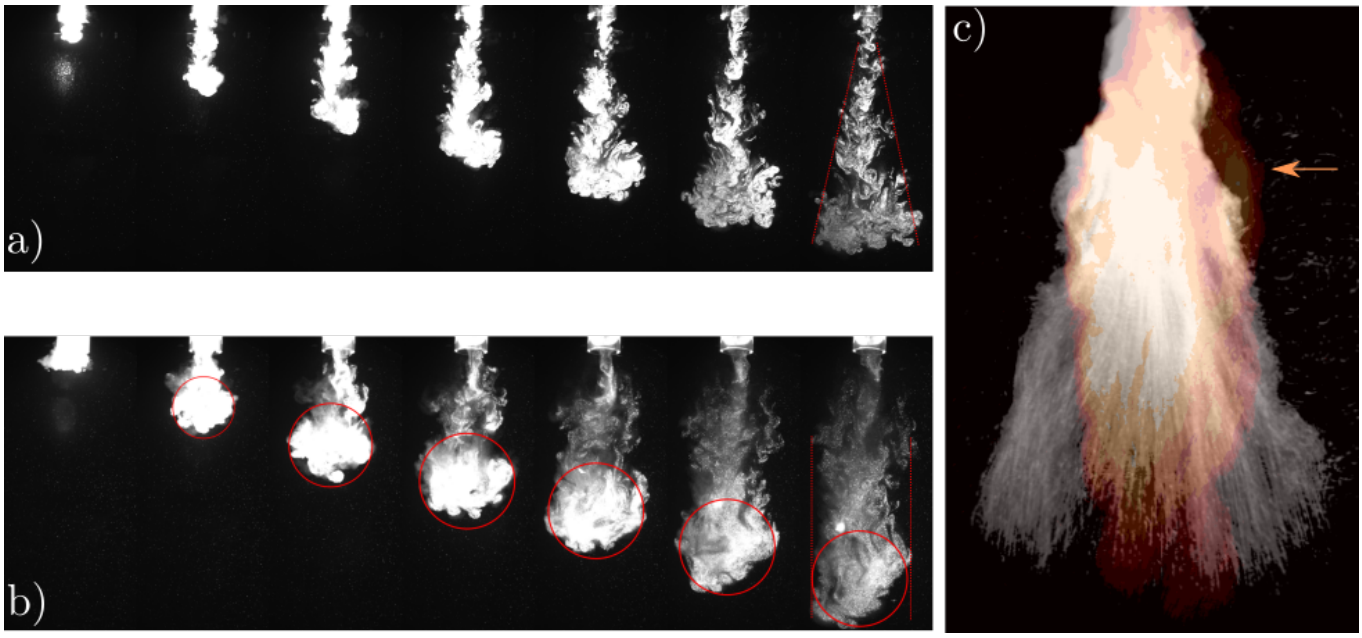

FIG. 2: Transition from the regime of turbulent thermal to the regime of vortical column. (a) Snapshots of a buoyant cloud of salt-water ($r_p = 0$) in the thermal regime ($\Omega = 0$, the time lapse between snapshots is 1s). (b) Snapshots of a buoyant cloud of small particles ($r_p = 29.9$ μm) in the vortical regime ($\Omega = 5$ rpm, the time lapse between snapshots is 1.7s). The red circles indicate the location of the frontal sphere; the dotted red lines show the growth of the thermal in (a) and the constant width of the vortical column in (b); the top cylinder has a diameter $D_{\rm cyl} = 3.2$ cm in (a) and (b). (c) Overlay of two integral images (pixel-by-pixel standard deviation of light intensity during the cloud fall) for particle clouds with $r_p = 64.4$ μm respectively at 0rpm (grey shades in the background) and 5rpm (orange shades). The arrow indicates the typical depth of transition to the vortical regime. The image height is 37.8 cm.

a. ***Onset of the columnar flow*** Our experiments showed that rotation interrupts the growth of the thermal at some depth $z_{\rm col}$, marking a transition from the regime of turbulent thermal to a vortical column of constant radial extension for $z \geq z_{\rm col}$. This transition is visible when comparing the linear growth of a thermal in the absence of rotation (figure 2a) with the constant width of the cloud when $\Omega = 5$ rpm (figure 2b). Integrated photographs in figure 2c further evidence the constant width of the cloud below some depth when $\Omega = 5$ rpm in orange. Initially the cloud inertia is large compared to rotation ($Ro(z) > 1$) and the cloud behaves as a non-rotating thermal (Morton et al. 1956): it grows linearly with depth (regime above the orange arrow in figure 2c or for $z_f < 22$ cm in figure 3a). Equation (7) predicts that, as the cloud radius r increases and its velocity decreases with depth, the local Rossby number decreases. When $Ro(z) = 1$, the Coriolis force becomes comparable to the cloud inertia and hence, the flow transitions towards a regime influenced by rotation. This defines the depth $z_{\rm col}$. This criterion of transition is illustrated with an example in figure 3a at depths $z_f > 22$ cm and we verify it for different particle radii r_p and rotation rates Ω in figure 3b. These results are consistent with past measurements in the literature for salt-water thermals falling in a rotating ambient (Ayotte and Fernando 1994, Fernando 1998, Helfrich 1994). All these studies

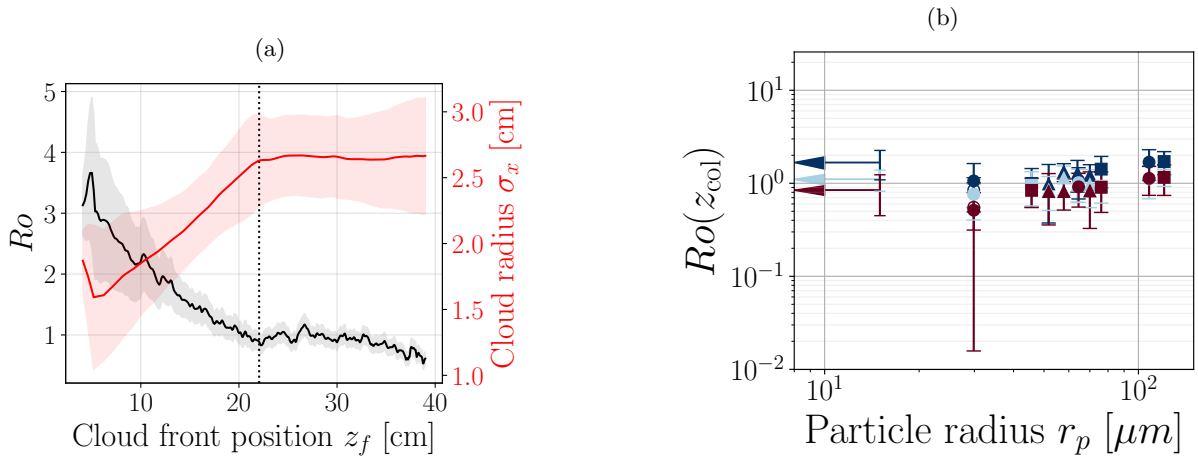

FIG. 3: (a) Rossby number $Ro(z)$ and experimental measure of the cloud radius $\sigma_x(z)$ (see Kriaa et al. (2022) for details) as a function of the position of the cloud front. In this experiment $\Omega = 5$ rpm and $r_p = 29.9$ μm. The transition to the vortical regime occurs at the depth shown by the vertical dotted line where $Ro(z_{\mathrm{col}}) = 1$ and the cloud radius becomes constant (see Kriaa et al. (2022) for details on measurements). (b) Average Rossby number after transition to the vortical regime for all rotation rates and particle sizes; adapted from figure 14 in Kriaa et al. (2022). The arrows point towards $\mathcal{R} = 0$ for salt water clouds, and the colour code is: (●) $\Omega = 5$rpm, (●) $\Omega = 10$rpm, (●) $\Omega = 20$rpm.

consistently show that the constant width of the column is the diameter of the turbulent thermal at depth z_{col} (as visible in figures 2c and 3a; see also figures 13 and 16 in Kriaa et al. (2022)).

We also observe that vortical columns penetrate through the solid body rotation with a constant front velocity. This explains why $Ro(z)$ remains close to 1 when $z > z_{\mathrm{col}}$ in figure 3a (see figures 18a, 18b and 19 in Kriaa et al. (2022) for more details). In addition, the vortical column is made of two different regions: (1) a frontal region (see the red circles in figure 2b), that we will assume spherical for simplicity, which corresponds to the former turbulent thermal and which no longer grows due to entrainment; (2) a columnar wake of particles detrained from the frontal sphere, which settle much slower than the frontal sphere (see figure 19 in Kriaa et al. (2022)).

b. ***Comparison with previous studies on columnar rotating flows*** When a rotating flow is dominated by the Coriolis force and the pressure gradient, these forces impose a geostrophic balance. Under these conditions, the flow is invariant along the rotation axis and forms columnar structures, the so-called Taylor columns (Maxworthy 1970, Taylor 1922).

The vortical columns we observe in our experiments when $Ro(z) < 1$ are reminiscent of Taylor columns. Our experiments are consistent with past studies on the formation (Davidson et al. 2006) and dynamics of such columns. The constant speed at the column front agrees with a drag force proportional to the falling speed and balancing the buoyancy force. Similar dynamics were predicted for an object falling along the axis of rotation in a bounded

or unbounded domain (Maxworthy 1970, Moore et al. 1969, Vedensky and Ungarish 1994). In the latter case the constant cloud velocity reads $\dot{z}_\infty \propto (\rho/\rho_f - 1)g/\Omega$ (see Bush et al. 1995, Moore et al. 1969, Stewartson 1952). As the object moves along the vertical axis, it stretches vortex tubes downstream and generates a converging flow and a cyclonic swirl in a Taylor column behind the object. In this column, the amplitude of the swirling flow $v_{\text{swirl}} \sim \dot{z}_\infty$ (Bush et al. 1995).

Note that these results hold for $Ro \ll 1$. When the cloud Rossby number is on the order of unity, the vertical extent of the Taylor column decreases (Maxworthy 1970, Minkov et al. 2002). Minkov et al. (2002) showed that the column behaves as if it were in an unbounded domain as long as inertial waves do not have enough time to propagate away from the moving cloud and reflect back to it, consistently with the interpretation of Greenspan (1968). Since our particle clouds verify $Ro(z \geq z_{\text{col}}) = 1$, the waves having the largest group velocity propagate as fast as the cloud falls. Consequently, these waves cannot propagate the information before the cloud reaches the bottom of the domain. This suggests that these clouds behave as if they were in an unbounded domain, falling with a velocity that scales like $\dot{z}_\infty \propto (\rho/\rho_f - 1)g/\Omega$.

In the light of these elements, we model a vortical column using the following assumptions. We consider that particle clouds penetrate through the ambient as a leading frontal sphere of constant radius r_{col} and with constant velocity $\dot{z}_f$. We also neglect the effect of the walls. We assume that particles are gradually detrained behind the frontal sphere, nourishing a cylindrical vortical column. The typical swirl velocity in the column is equal to the velocity of the frontal sphere $\dot{z}_f$, so that vertical motions stir the particles in the columnar flow. For simplicity we will assume that these motions are vigorous enough to homogenise the particle concentration in the vortical column. The next section presents a model of column growth that is consistent with these key points.

III. MODEL OF COLUMN GROWTH THROUGH DETRAINMENT

Based on the above experimental observations, we now derive a minimalist model for the evolution of a particle cloud in the presence of rotation. Figure 4 provides an illustration of this model. The cloud initially grows as a turbulent thermal (A). At depth z_{col}, $Ro = 1$ and the thermal transitions to a frontal sphere of constant radius and speed (B). Particles are detrained behind the falling sphere and into a swirling column (B). After some distance, the sphere has detrained all its particles in the swirling column (C). Eventually, particles will fall down to the bottom of the tank, possibly before the kinetic enegy of the column dissipates viscously (D). Particles can drag the fluid with them along their fall, or decouple from it, as we have seen in experiments. Which of these two configurations occurs

depends on subtle hydrodynamical interactions between particles that enable the interstitial fluid between them to be dragged downward. These aspects require further investigation, as discussed in section V. In this study, we speculate that particles drag a negligible amount of fluid when they decouple from the swirling column. Consequently, they rain out in quiescent liquid.

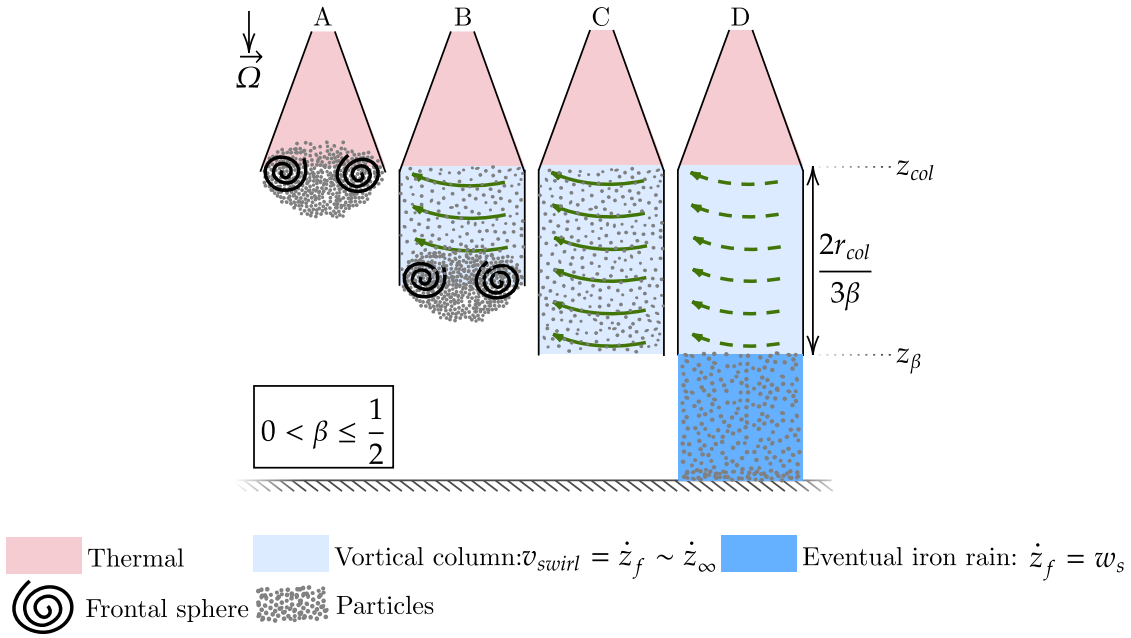

FIG. 4: Sketch of the cloud evolution. (A) The cloud initially grows as a turbulent thermal until $Ro(z) = 1$; (B) then the frontal sphere falls with constant speed while detraining particles in the swirling column; (C) all particles are detrained in the column of depth $2r_{\rm col}/3\beta$ and swirl with the fluid; (D) ultimately, because of gravitational drift (i.e. settling) and viscous dissipation, particles rain out of the column until reaching the bottom where they accumulate.

By analogy with models of entrainment (Morton et al. 1956), the detrainment (de Rooy et al. 2013, Taylor and Baker 1991) of particles into the columnar wake is modelled through a single coefficient of detrainment β which is analogous to the coefficient of entrainment α (Baines 2001, de Rooy and Siebesma 2008). The coefficient of detrainment β is the ratio of the outward velocity transporting particles out of the spherical frontal blob, over the downward velocity of the cloud. The mass conservation of particles then reads

$$\frac{d}{dt}\left[\frac{4}{3}\pi r_{\rm col}^3 \phi \rho_p\right] = \frac{4}{3}\pi r_{\rm col}^3 \rho_p \frac{d\phi}{dt} = -2\pi r_{\rm col}^2 \beta \dot{z}_f \phi \rho_p, \tag{8}$$

where the only unknown $\phi(t)$ is the particle volume fraction within the frontal sphere of downward velocity $\dot{z}_f$ and radius $r_{\rm col}$. The term $(\beta \dot{z}_f)$ is the detrainment velocity taking particles out of the cloud. The factor $2\pi r_{\rm col}^2$ on the right-hand side indicates that detrainment is considered to happen only on the upper half of the frontal sphere. Taking $t = 0$ when the cloud is at depth $z_{\rm col}$, the solution of this Ordinary Differential Equation (ODE) reads

$$\phi(t) = \phi(t=0)\exp\left[-\frac{t}{\tau_\beta}\right] \iff \phi(z) = \phi(z_{\rm col})\exp\left[-\frac{3\beta(z-z_{\rm col})}{2r_{\rm col}}\right], \tag{9}$$

where

$$\tau_\beta = \frac{2r_{\rm col}}{3\beta\dot{z}_f} \tag{10}$$

is the characteristic duration of detrainment. Hence the column completes detrainment in a time of order τ_β. Since the column front moves with constant velocity $\dot{z}_f$, the column height after complete detrainment is of order $\dot{z}_f\tau_\beta = 2r_{\rm col}/3\beta$ and the depth of complete detrainment

$$z_\beta = z_{\rm col} + \frac{2r_{\rm col}}{3\beta}. \tag{11}$$

Particles are always detrained in the column behind the frontal sphere, hence $\beta > 0$. The maximum value for β is determined with a geometrical argument. During a time dt, the frontal sphere detrains buoyant material in a volume $2\pi r_{\rm col}^2\beta\dot{z}_f dt$; in the meantime the column grows by a volume $\pi r_{\rm col}^2\dot{z}_f dt$; equating them yields $\beta = 1/2$ as an upper bound. With this value, a frontal sphere of volume $4\pi r_{\rm col}^3/3$ typically detrains its particles in an identical volume $\pi r_{\rm col}^2(4r_{\rm col}/3) = 4\pi r_{\rm col}^3/3$ (see equation (11) for $\beta = 1/2$), meaning the sphere only adapts its shape to become a cylinder of radius $r_{\rm col}$ and depth $4r_{\rm col}/3$.

The range $0 < \beta < 1/2$ corresponds to the sketch in figure 4. Particles are detrained in a column of large depth-to-radius ratio. In this case, the volume of material detrained by the frontal sphere is lower than the volume gained by the vortical column. This implies that the volume of the column is complemented by ambient fluid through entrainment, likely in the near wake of the frontal sphere where the flow converges towards the column (see section II C 2 b). Additionally, since the frontal sphere keeps a constant volume while detraining both fluid and particles, the sphere also entrains new ambient fluid that compensates the detrained volume.

In our experiments, we observe that detrainment of the frontal sphere ends at depths in the range $[45 - 90]$ cm. Our columns had a width $r_{\rm col}$ given by $\sigma_x(z_{\rm col})$, which varied with Ω but was typically of order $r_{\rm col} \sim 2D_{\rm cyl}$, hence equation (11) yields $\beta \in [0.05 - 0.12]$, a range that is consistent with typical values quantifying entrainment for

turbulent jets and plumes (e.g. Carlotti and Hunt 2017, Turner 1986, van Reeuwijk and Craske 2015, Wang and Law 2002). A larger β value translates into a weaker effect of rotation (see Appendix B). B.

According to equation (9), the column is nourished by the frontal sphere with a mass flux of detrained particles that decays exponentially in depth. Yet, our visualisations in a vertical laser sheet evidence no stratification in the vortical column. This observation suggests that the buoyant material is substantially stirred by turbulent motions in the column. To keep our model as simple as possible, we assume that stirring is sufficient behind the frontal sphere to neglect heterogeneities within the vortical column, so that its concentration is uniform.

IV. IMPLICATIONS FOR MIXING AND EQUILIBRATION AFTER A PLANETARY IMPACT

In this section, we apply our experimental results to the fall of liquid metal into a magma ocean following a planetary impact. We use the following notations (see a list in table II): the densities of metal ρ_m and silicates ρ_s, their respective kinematic viscosities (ν_m and ν_s) and mass diffusivities (κ_m and κ_s), the angular velocity Ω of the target planet, the radius R_t of the target planet, the radius R of the impactor, and f_m the volume fraction of metal within the impactor; we use the value $f_m = 0.16$ that corresponds to the same core fraction as in the present-day Earth. The acceleration of gravity g is assumed uniform in the magma ocean (see Fig. 5b in Olson 2015).

Quantity	Notation	Value	Reference
Density of metal	ρ_m	7800 kg.m^{-3}	Lherm and Deguen (2018)
Density of silicates	ρ_s	3500 kg.m^{-3}	Qaddah et al. (2019)
Kinematic viscosity of metal	ν_m	1.28×10^{-6} m^2.s^{-1}	Lherm and Deguen (2018)
Kinematic viscosity of silicates	ν_s	1.43×10^{-5} m^2.s^{-1}	Karki and Stixrude (2010)
Mass diffusivity of metal	κ_m	10^{-8} m^2.s^{-1}	Deguen et al. (2014), Lherm and Deguen (2018)
Mass diffusivity of silicates	κ_s	10^{-8} m^2.s^{-1}	Deguen et al. (2014), Lherm and Deguen (2018)
Metal volume fraction in the impactor	f_m	0.16	Landeau et al. (2021)
Radius of the target planet	R_t	6371 km	Kono (2010)
Angular velocity of the target planet	Ω	$2\Omega_\oplus - 5\Omega_\oplus$	-
Radius of the impactor	R	$\leq R_t/3$	-
Acceleration of gravity	g	$0.25g_\oplus - 2g_\oplus$	-

TABLE II: Governing quantities in the context of metal-silicate mixing following a planetary impact. The last three lines give ranges for the parameters that are varied, with $\Omega_\oplus = 7.3 \times 10^{-5}$ rad.s^{-1} and $g_\oplus = 9.81$ m.s^{-2}.

Both Ω and g are varied in the next sections; the subscript $\oplus$ denotes the values on Earth today. The constant entrainment coefficient is fixed to $\alpha = 0.25$ (Deguen et al. 2014, Landeau et al. 2021). In this study, we aim at demonstrating that rotation can affect metal-silicate equilibration after an impact. To be conservative, we therefore use the end-member value $\beta = 0.12$ in what follows. Results for the lower end-member $\beta = 0.05$ are given in Appendix

B.

Finally, during an impact the metal of the impactor mixes with silicates from the target planet so that the metal dilutes in a larger volume, with an effective radius r_0 (Landeau et al. 2021). In all that follows, we assume that impactors approach the target planet at the escape velocity and we account for mixing during an impact using the scaling law from Landeau et al. (2021) that relates the radius of the impactor R with the radius of the thermal as it starts sinking r_0. Past studies have shown that the impactor core behaves as a turbulent thermal of radius r_0 immediately after an impact (Deguen et al. 2014, Landeau et al. 2021, Wacheul and Le Bars 2018).

For simplicity we consider that the cloud contains spherical drops from the very start of its fall. The experiments of Landeau et al. (2021) suggest that, after an impact, the impactor core fragments after less than 7.5 times its initial radius (see figure 14 in Landeau et al. 2021). For such breakup lengths, Deguen et al. (2014) predict that the drop size is less than 4 mm (see their figure 7 and the discussion in section 8). Therefore, we focus in the next sections on the representative case $r_p = 10^{-3}$ m. With these assumptions, we use the model introduced in section III to compute the mixing and the efficiency of equilibration as a function of the impactor size and the magma ocean depth. We show depths down to the position of the present-day CMB i.e. $z/R_t \simeq 0.45$ except when analysing the equilibration efficiency: indeed, to analyse data in a more general way, and since the position of the CMB is unknown during accretion, the depth z extends down to the centre of the target planet in figures 8, 9, 12 and 13.

A. Regimes in a magma ocean for a cloud of millimetric drops

Figure 5a shows the different regimes experienced by a falling cloud of millimetre-sized drops for various impactor-to-target radius ratios R/R_t up to a depth corresponding to the present-day core-mantle boundary in Earth. The solid blue line marks the depth $z_{\rm col}$ where clouds transition to a vortical column for $g = g_\oplus$ and $\Omega = 2\Omega_\oplus$. Such rotation rates in the early Earth are suggested by estimates of the tidal dissipation of the Earth-Moon system (Daher et al. 2021, Touma and Wisdom 1994). The dashed dark line in figure 5a marks the transition to the regime of iron rain.

We observe that the larger the impactor-to-target radius ratio R/R_t, the larger the initial buoyancy of the cloud of droplets, the larger the cloud inertia, hence the deeper the transition from the thermal to the vortical column. On Earth, the fall of an impactor smaller than about $R/R_t \simeq 7.2 \times 10^{-2}$, i.e. smaller than $R = 459$ km, is influenced by rotation before reaching the present-day CMB at $z = 0.45R_t$ (see the blue line in figure 5a). In this case, if the magma ocean is deep, rotation may affect the flow and therefore the efficiency of chemical equilibration. Conversely,

impactors in the range $R/R_t \geq 7.2 \times 10^{-2}$ reach the core-mantle boundary before ever transitioning to the regime of vortical column. Such clouds always behave as turbulent thermals.

When $R/R_t \leq 5.0 \times 10^{-3}$ (left of the red solid line), impactors have so little initial buoyancy that their Rossby number is never larger than unity. Consequently they experience the influence of background rotation from the very start of their fall. This scenario is consistent with the numerical simulation of a polar impact by Maas et al. (2021).

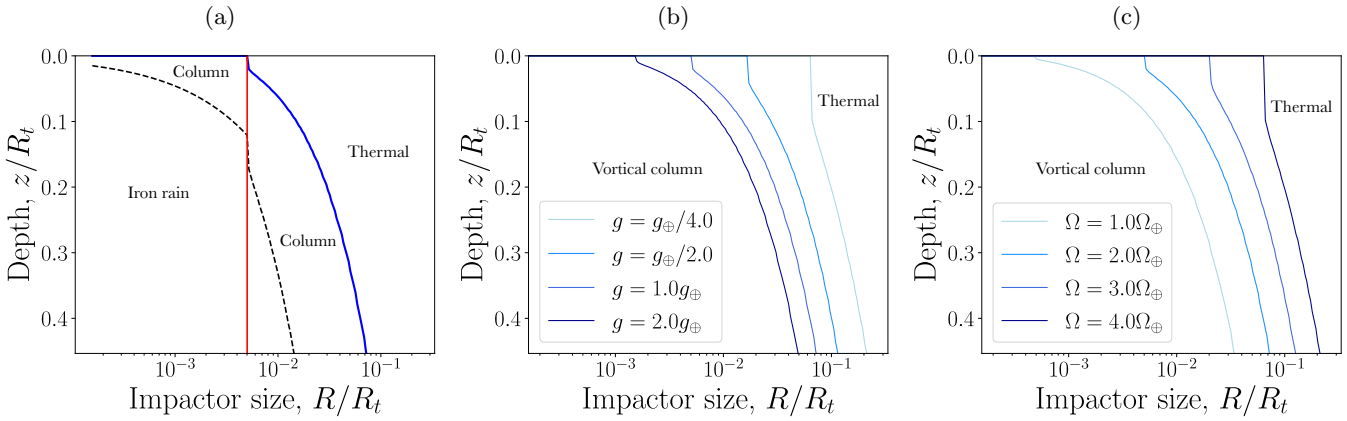

FIG. 5: (a) Dynamical regimes of a cloud of millimetre-sized drops for various impactor-to-target radius ratios for $\Omega = 2\Omega_\oplus$. Transitions correspond to the depth $z_{\rm col}$ (——) and the depth of complete detrainment z_β for $\beta = 0.12$ (- - -). Clouds in the range $R/R_t \leq 5.0 \times 10^{-3}$ verify $z_{\rm col} = 0$ because their Rossby number remains below unity at all depths; they are separated from other clouds by the vertical solid red line (——). (b) Influence of gravity on the transition from a thermal to a vortical column at $z = z_{\rm col}$; the angular velocity is $\Omega = 2\Omega_\oplus$. (c) Influence of the angular velocity on the same transition; the gravity is $g = g_\oplus$.

If the magma ocean is sufficiently deep for detrainment to complete, the clouds transition from the vortical regime to the regime of iron rain. How does this transition happen? After detrainment, iron drops swirl with the fluid inside the wake at most until viscosity has fully dissipated the swirl. Let us show that in practice, iron drops rain out of the vortical column before the swirl is dissipated. While iron drops are spiralling azimuthally, they keep settling downwards because of gravity with velocity w_s, as can be derived from the momentum equation of an individual drop. The time required for the topmost drops to settle down to the bottom of the vortical column is the ratio of the column height over the settling velocity w_s. This timescale is compared to the timescale of viscous dissipation $r_{\rm col}^2/\nu_s$ of the vortical column, and to the shorter timescale $\Omega^{-1}Ek^{-1/2}$ that should be taken into account if Ekman pumping develops in the magma ocean (Greenspan 1968), with $Ek = \nu_s/\Omega z_{\rm ocean}^2$ the Ekman number based on the depth $z_{\rm ocean}$ of the magma ocean. For millimiter-sized drops, and for all possible sizes of $R < R_t$ hitting a planet of gravity $g = g_\oplus$ and angular velocity $\Omega = 2\Omega_\oplus$, the settling timescale is 4-5 orders of magnitude lower than $\Omega^{-1}Ek^{-1/2}$ which is itself

2-3 orders of magnitude lower than $r_{\rm col}^2/\nu_s$. Therefore iron drops are expected to rain out of the wake before the swirl is dissipated. This conclusion also held in our experiments (Kriaa et al. 2022): our slowest particles ($\mathcal{R} = 7.57 \times 10^{-2}$) settled over the column height in about 2.5 min which was an order of magnitude lower than $\Omega^{-1} Ek^{-1/2}$, hence we observed that particles rained out of the vortical column before the dissipation of the swirl. In this situation, we call 'iron rain' the regime below the dashed dark line in figure 5a, when drops settle after detrainment from a vortical column.

The transition to iron rain is delayed for larger impactors because the larger they are, the wider the vortical columns ($r_{\rm col}$) and the deeper the depth $z_{\rm col}$, hence the deeper the depth of complete detrainment $z_{\rm col} + 2r_{\rm col}/3\beta = z_\beta$. This depth turns out to be deeper than the present-day core-mantle boundary for $R/R_t \geq 1.4 \times 10^{-2}$ (see the dashed line in figure 5a) .

Gravity g and the angular velocity Ω of the target planet are important parameters affecting the transition from the thermal to the swirling column stage. Their respective influence is illustrated in figure 5b and figure 5c. For a given impactor-to-target radius ratio, the larger gravity the deeper the depth of transition $z_{\rm col}$. As g increases, the cloud velocity increases during its phase of acceleration. It therefore takes a larger cloud radius $r_{\rm col} = r_0 + \alpha z_{\rm col}$ for the Coriolis force to overcome the cloud inertia and verify the condition $Ro = 1$. Thus, the transition to a vortical column is delayed deeper in the magma ocean. Figure 5c shows that the faster the background rotation Ω, the shallower the depth $z_{\rm col}$. This is straightforward from the definition of the Rossby number $Ro \propto \Omega^{-1}$: for a given impactor on a target planet of given gravity, the larger the angular velocity Ω the earlier the Coriolis force overcomes the cloud inertia to verify $Ro = 1$, hence $z_{\rm col}$ decreases. Consistently, when g decreases and Ω increases, larger and larger impactors are subject to the influence of rotation from the very start of their fall at depth $z = 0$ (figures 5b and 5c). On a fast-spinning Earth with $\Omega > 5\Omega_\oplus$ as proposed by Ćuk and Stewart (2012), the transition to a vortical column cannot be shown since the rotation affects all the impactors we consider from the very surface of the Earth.

B. Equilibration in a magma ocean

1. Definitions of mixing and equilibration efficiency

As a cloud of metal drops falls in the magma ocean, the metal phase is stirred with silicates. This favours chemical transfers between the two phases. The present section models this equilibration between metal and silicates on the basis of previous studies (Deguen et al. 2014, Landeau et al. 2021), but including the effect of rotation and the regime

of swirling columns.

We quantify mass transfers using the *equilibration efficiency* (Deguen et al. 2014, Landeau et al. 2021). This quantity compares the very initial state when no mass transfer has happened yet, to a state of thermodynamic equilibrium between the metal phase of the impactor and a given mass of silicates. For a chemical element i (e.g. tungsten), the equilibration efficiency is the ratio of the mass $\mathcal{M}_i$ of i transferred between these two states, over the maximum mass $\mathcal{M}_{\rm i,max}$ that could be transferred if (1) the metal was diluted in an infinite volume of silicates and (2) all the metal of the impactor fully equilibrated. Consequently the equilibration efficiency reads (Deguen et al. 2014)

$$\mathcal{E}_i(z) = \frac{\mathcal{M}_i(z)}{\mathcal{M}_{\rm i,max}} = \frac{m_m(z)|c_m^{\rm eq}(z) - c_m^0|}{\mathcal{M}_{\rm i,max}}, \tag{12}$$

with $m_m(z)$ the mass of metal that equilibrates, c_m^0 the initial mass concentration of element i in the metal, and $c_m^{\rm eq}(z)$ the concentration of i in the metal when thermodynamic equilibrium is reached. In the following the quantity $\mathcal{E}_i(z)$ will simply be referred to as the 'efficiency'.

From its definition, the efficiency is a 'state function' in the sense that it only depends on both the initial and final states of metal and silicates, not on the thermodynamic path that connects these states. Thus, the efficiency (12) quantifies chemical transfers provided that a thermodynamic equilibrium is reached by metal and silicates during the cloud fall, and that the cloud is uniform in composition. These conditions are assumed in our next calculations and discussed in Appendix C.

a. ***Efficiency of turbulent thermals*** In the case of turbulent thermals, previous studies (Deguen et al. 2014) have already established that the equilibration efficiency reads

$$\mathcal{E}_i^{\rm th}(z) = \frac{k}{1 + \frac{D_i}{\Delta_{\rm th}(z)}}, \tag{13}$$

where the quantity $\Delta_{\rm th}(z)$ is the *metal dilution*, defined as the ratio of the mass of silicates over the mass of metal contained in the thermal (Deguen et al. 2014). The dilution increases with depth as (Landeau et al. 2021)

$$\Delta_{\rm th}(z) = \frac{\rho_s}{\rho_m}\left[\left(\frac{r_0 + \alpha z}{R}\right)^3 \frac{1}{f_m} - 1\right], \tag{14}$$

with ρ_s the density of silicates, ρ_m the density of metal, r_0 the initial thermal radius, α the coefficient of entrainment, z the cloud depth, R the radius of the impactor, and f_m the volume fraction of metal in the impactor.

In equation (13), the superscript 'th' distinguishes between the general notation $\mathcal{E}_i(z)$ and the efficiency $\mathcal{E}_i^{\rm th}(z)$ of turbulent thermals specifically, since this latter efficiency serves as a reference for mass transfers. In equation (13), k is the mass fraction of impactor core that equilibrates chemically. Its value can be lower than unity, for example if the liquid metal is not vigorously stretched by the turbulence, which would allow some fraction of the impactor core to keep its initial composition. Based on the conclusions of Deguen et al. (2014), we will consider that the entire impactor core equilibrates with silicates, hence we set $k = 1$ in our estimates of the efficiency. In equation (13), D_i is the partition coefficient of element i, that is to say the ratio between the concentration (in weight %) of i in the metal to the concentration of i in the silicates, both considered *at thermodynamic equilibrium*. Because the pressure, temperature and partial pressure of oxygen vary as planets grow, the partition coefficient of a single element can vary by several orders of magnitude. Yet, it is useful to give the typical range of D_i for some elements: the partition coefficient of gallium is on the order of unity (Righter 2011), that of nickel and cobalt varies from ~ 10 to several hundreds during Earth's accretion (Fischer et al. 2015, Siebert et al. 2012), that of tungsten is typically in the range 10-10^3 (Jennings et al. 2021, Righter 2011), that of palladium is on the order of 10^4 (Righter et al. 2018), and that of gold is larger than 10^3 (Righter et al. 2018). Here we explore values of D_i ranging from 1 to 10^4.

b. ***Efficiency of vortical columns*** Equation (13) also applies to the columnar regime after substituting the general notation $\mathcal{E}_i(z)$ for $\mathcal{E}_i^{\rm col}(z)$, and replacing the metal dilution of a thermal $\Delta_{\rm th}(z)$ by its equivalent expression $\Delta_{\rm col}(z)$ in the regime of vortical column:

$$\mathcal{E}_i^{\rm col}(z) = \frac{k}{1+\frac{D_i}{\Delta_{\rm col}(z)}}, \tag{15}$$

where we assume $k = 1$ as before. The mass of metal involved in chemical transfers is unchanged in this regime, however the mass of silicates now includes those present in the frontal sphere and those present in the wake, so that the metal dilution reads

$$\Delta_{\rm col}(z) = \underbrace{\frac{\rho_s}{\rho_m}\left[\left(\frac{r_0+\alpha z_{\rm col}}{R}\right)^3\frac{1}{f_m}-1\right]}_{\Delta_{\rm th}(z_{\rm col})} + \frac{3\rho_s}{4\rho_m}\frac{(z-z_{\rm col})r_{\rm col}^2}{f_m R^3}, \tag{16}$$

which is applicable for $z_{\rm col} \leq z \leq z_\beta$. In equation (16) the terms on the right-hand side respectively correspond to the metal dilution $\Delta_{\rm th}(z_{\rm col})$ of a turbulent thermal at the depth $z_{\rm col}$, and to the metal dilution within the vortical column.

c. ***Efficiency of an iron rain*** As soon as metal drops have separated from silicates, one can no longer define a volume of silicates that would accompany the metal drops and mix with them during their fall. Instead, drops cross an ever-renewed volume of silicates and deposit (or absorb) some element i in the quiescent magma ocean, thus modifying the profile of concentration of i with respect to its initially uniform value c_s^0. Therefore no metal dilution is defined in this regime. Mass transfers are quantified by the evolution of the concentration in element i within the metal drops. Since mass transfers are transient during this regime of iron rain, no equilibrium concentration is reached in the drops, so the equilibration efficiency now reads

$$\mathcal{E}_i^{\rm rain}(z) = \frac{\mathcal{M}_i(z)}{\mathcal{M}_{\rm i,max}} = \frac{m_m(z)|c_m(z) - c_m^0|}{\mathcal{M}_{\rm i,max}}, \tag{17}$$

where the superscript 'eq' has been removed from the concentration $c_m(z)$ in the metal drops. Modelling of transfers between a settling spherical drop and the surrounding ambient liquid has been investigated in several studies (Lherm and Deguen 2018, Qaddah et al. 2019, Samuel 2012, Ulvrová et al. 2011, Wacheul and Le Bars 2018). From mass conservation and after modelling the diffusive flux at the metal-silicates interface, these studies show that the concentration in element i varies exponentially in depth to reach the equilibrium concentration $D_i c_s^0$ on a characteristic length scale $l_{\rm eq}$ called the 'equilibration length scale'. For a spherical drop, Lherm and Deguen (2018) established that this length scale reads (see their equation 36 and appendix C)

$$l_{\rm eq} \sim w_s \frac{r_p^2 D_i}{6\kappa_s} Pe^{-1/2} \left(1 + \frac{1}{D_i}\sqrt{\frac{\kappa_s}{\kappa_m}}\right), \tag{18}$$

with $Pe = r_p w_s/\kappa_s$. With this, one can establish the expression of the efficiency in the iron rain regime, as detailed in appendix E. The final expression of the efficiency reads

$$\mathcal{E}_i^{\rm rain}(z) = 1 + [\mathcal{E}_i(z_\beta) - 1] \exp\left(-\frac{z - z_\beta}{l_{\rm eq}}\right). \tag{19}$$

which is applicable for $z > z_\beta$. Consistently, the efficiency is continuous at depth z_β, and it evolves towards a state of complete mass transfer when z goes to infinity since $\mathcal{E}_i(z) \underset{z\to\infty}{\longrightarrow} 1$. Interestingly, in the thermal and vortical column regimes, the size of drops had no influence on equilibration. However in the present regime of iron rain, the drop size explicitly determines the efficiency $\mathcal{E}_i^{\text{rain}}(z)$ through l_{eq}, whose value for $r_p = 10^{-3}$ m is 2 m, 20 m and 200 m respectively when D_i is equal to 10^2, 10^3 and 10^4.

To minimise notations, in the following the efficiency is always denoted with the general notation $\mathcal{E}_i(z)$ defined as

$$\mathcal{E}_i(z) = \begin{cases} \mathcal{E}_i^{\text{th}}(z), & \text{if } z < z_{\text{col}} \\ \mathcal{E}_i^{\text{col}}(z), & \text{if } z_{\text{col}} \leq z \leq z_\beta \\ \mathcal{E}_i^{\text{rain}}(z), & \text{if } z > z_\beta \end{cases} . \tag{20}$$

Similarly the metal dilution is denoted under the general form $\Delta(z)$, which corresponds to $\Delta_{\text{th}}(z)$ in the thermal regime and to $\Delta_{\text{col}}(z)$ in the columnar regime.

C. Dilution and mixing

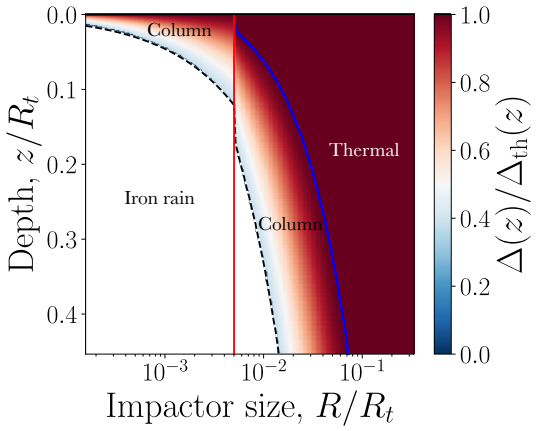

FIG. 6: Evolution of the ratio of metal dilution $\Delta(z)/\Delta_{\text{th}}(z)$ along depth z in the magma ocean for several impactor sizes, where Δ is the mass of equilibrated silicates divided by the mass of impactor metal and Δ_{th} is the value of Δ for a pure thermal i.e. in the absence of rotation. Transitions correspond to $Ro(z_{\text{col}}) = 1$ (——) and to $z = z_\beta$ (- - -) for $\beta = 0.12$. The dilution Δ is not defined in the iron rain regime so it is masked in white. The solid red line separates the impactors that are influenced by rotation in the aftermath of the impact (on the left-hand side) from those that are affected by rotation deeper in the mantle (on the right-hand side)

Focusing on mixing in thermals and vortical columns, the metal dilution $\Delta(z)$ is computed at any depth for all drop sizes. Past studies which neglected the influence of planetary rotation showed that particles are expected to remain

in a turbulent thermal from the start to the end of their fall in the magma ocean (Deguen et al. 2014, 2011, Landeau et al. 2021). Consequently the metal dilution $\Delta(z)$ is compared to the value $\Delta_{\rm th}(z)$ which would be experienced by the cloud if planetary rotation had no influence on its dynamics. Results are shown in figure 6. By definition, $\Delta(z)/\Delta_{\rm th}(z) = 1$ where clouds behave as turbulent thermals.

In figure 6, we observe that dilution reduces in the columnar regime. This originates from the slower growth of vortical columns compared to thermals: along a depth increment dz, the ratio of the volume increment of a turbulent thermal of radius r over the volume increment of a column of radius $r_{\rm col}$ is $4\alpha(r/r_{\rm col})^2 \simeq (r/r_{\rm col})^2$. So the deeper the vortical column, the larger the deviation between $\Delta(z)$ and $\Delta_{\rm th}(z)$.

D. Efficiency of equilibration

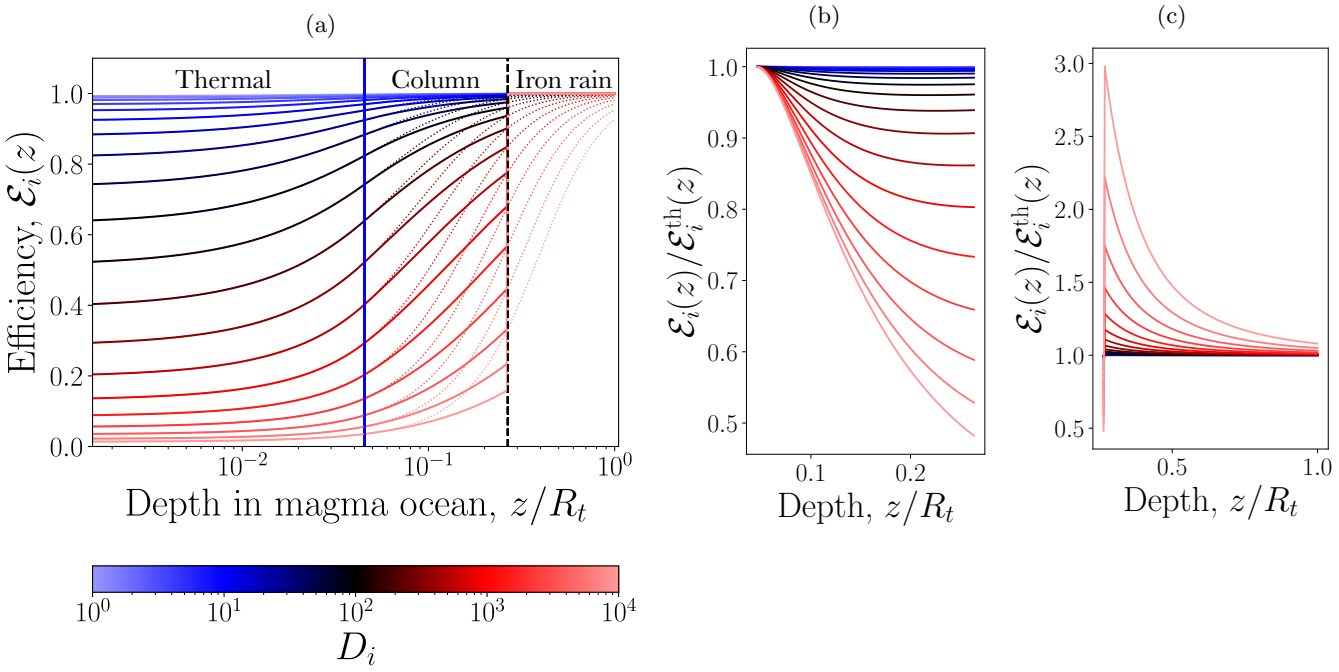

FIG. 7: Evolution of the efficiency for an impactor of radius $R = 50$ km hitting the planet Earth ($R_t = 6371$ km, $\Omega = 2\Omega_\oplus$, $g = g_\oplus$, $\beta = 0.12$). (a) Solid curves show the efficiency $\mathcal{E}_i(z)$, while thin dotted lines show the evolution of $\mathcal{E}_i^{\rm th}(z)$ for reference. Vertical lines indicate the depth $z_{\rm col}$ (——) and the depth z_β (- - -). The next two figures show the evolution of the ratio $\mathcal{E}_i(z)/\mathcal{E}_i^{\rm th}(z)$ (b) in the vortical regime and (c) in the iron rain regime. The size of drops is fixed to $r_p = 10^{-3}$ m.

The equilibration efficiency $\mathcal{E}_i(z)$ computed from equations (13)-(20) is shown in figure 7a for an impactor of radius $R = 50$ km falling onto Earth. The value of the equilibration efficiency at the surface of the planet ($z/R_t = 0$) is positive because we account for the dilution occurring during the impact (Landeau et al. 2021). It also varies with

D_i consistently with equation (13): the lower the partition coefficient D_i, i.e. the less siderophile the element i, the larger the efficiency $\mathcal{E}_i^{\rm th}(z=0)$.

As the cloud of drops falls deeper in the magma ocean, it dilutes more and more so the efficiency always increases with depth. Once the cloud goes beyond the depth $z_{\rm col}$ (vertical solid blue line), it transitions to the regime of vortical columns, which is less efficient than turbulent thermals at diluting the metal drops. Hence, at a given depth, the slope of the curve $\mathcal{E}_i(z)$ is smaller than that of thermals (dotted lines) until the cloud reaches the depth of complete detrainment z_β.

Importantly, the final value of the equilibration efficiency is that recorded at the bottom of the magma ocean. If a cloud reaches the bottom of the magma ocean while it is in the vortical regime, then accounting for planetary rotation leads to a decrease in the equilibration efficiency. This is even clearer in figure 7b, which compares the efficiency $\mathcal{E}_i(z)$ of a cloud in the vortical regime with the reference value $\mathcal{E}_i^{\rm th}$ of a turbulent thermal at the same depth. The efficiency is always reduced in the vortical regime ($\mathcal{E}_i(z)/\mathcal{E}_i^{\rm th}(z)<1$) and the discrepancy between the actual efficiency $\mathcal{E}_i(z)$ and that of a thermal reaches 50% at depth $z=0.26R_t$ for highly siderophile elements with $D_i=10^4$.

When $z>z_\beta$ (on the right of the vertical dashed dark line in figure 7a), the regime of iron rain ensures a rapid equilibration and $\mathcal{E}_i(z)$ quickly reaches unity. Figure 7c shows that the ratio $\mathcal{E}_i(z)/\mathcal{E}_i^{\rm th}(z)$ becomes larger than unity for most partition coefficients: despite the reduction of equilibration in the vortical regime, mass transfers are so efficient in the regime of iron rain that this delay is caught up and $\mathcal{E}_i$ becomes larger than $\mathcal{E}_i^{\rm th}$.

The previous conclusions are generalised in figures 8a-8c which show the evolution of the efficiency $\mathcal{E}_i(z)$ along depth for various impactor-to-target radius ratios R/R_t. For all impactors, the efficiency slowly increases with depth until $z=z_\beta$, where the iron rain regime abruptly leads to $\mathcal{E}_i=1$. Figures 8d-8f show the ratio $\mathcal{E}_i(z)/\mathcal{E}_i^{\rm th}(z)$ as a function of depth. Expectedly, the ratio is equal to unity at depths $z\leq z_{\rm col}$ in the thermal regime. Then, the ratio lowers in the vortical regime until the depth z_β. Finally, equilibration is so fast in the iron rain regime that the ratio $\mathcal{E}_i(z)/\mathcal{E}_i^{\rm th}(z)$ becomes larger than unity for $z>z_\beta$, all the more so as D_i is larger. Consequently, modelling clouds as turbulent thermals at all depths is all the more inaccurate as elements are more siderophile. This is especially true for the largest impactors that transition to iron rain in figure 8f, where the efficiency $\mathcal{E}_i(z)$ largely overshoots $\mathcal{E}_i^{\rm th}(z)$ for $z>z_\beta$. Note that this dependency with respect to the size of the impactor is not due to the iron rain regime (the equilibration length $l_{\rm eq}$ is independent of the impactor size R/R_t) but to the lower efficiency $\mathcal{E}_i^{\rm th}(z)$ of turbulent thermals produced by larger impactors.

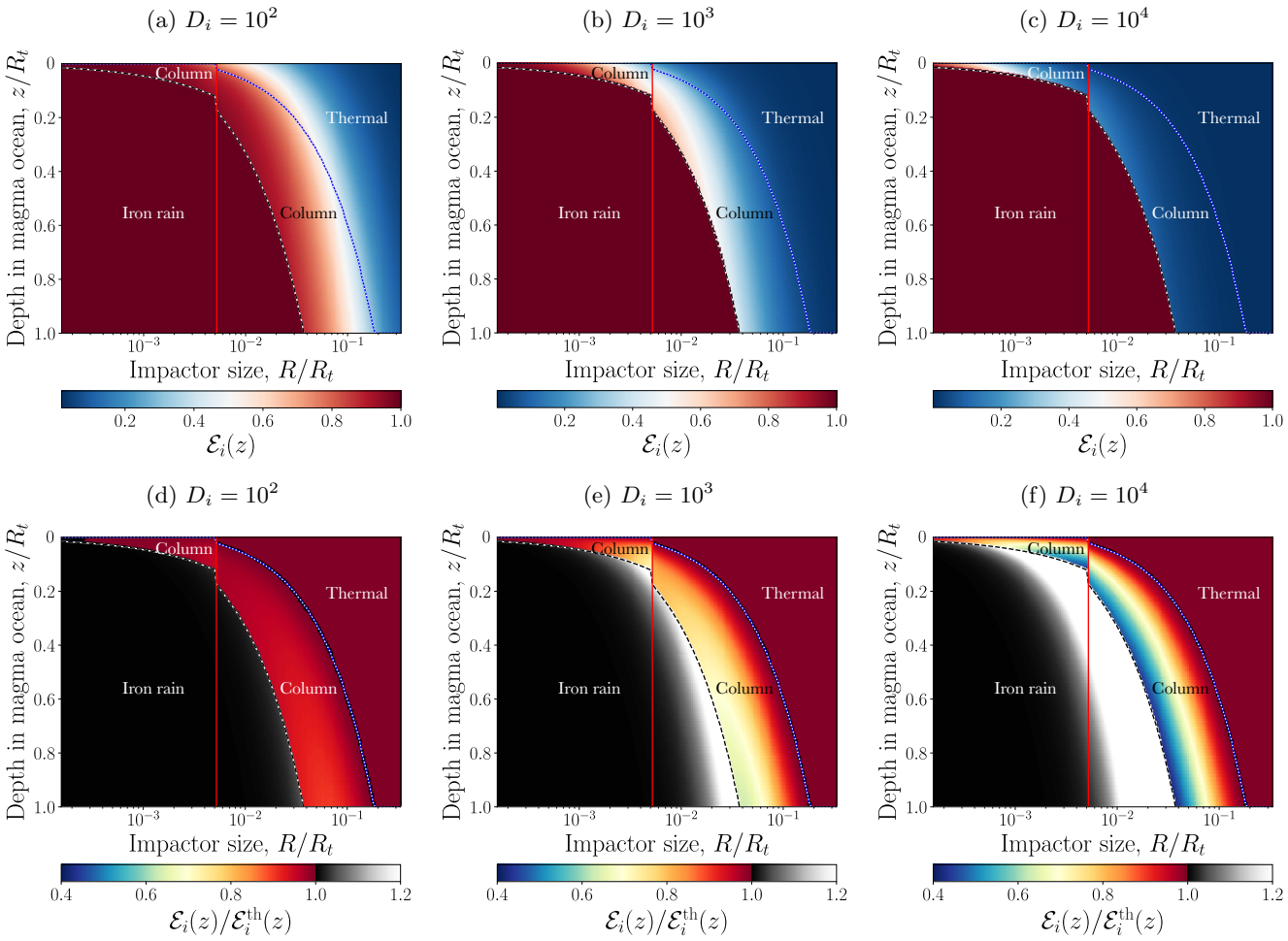

FIG. 8: Equilibration efficiency $\mathcal{E}_i$ (a-c) and ratio $\mathcal{E}_i/\mathcal{E}_i^{\rm th}$ (d-f) as a function of impactor size and magma ocean depth for partition coefficients $D_i = 10^2$ (a and d), $D_i = 10^3$ (b and e) and $D_i = 10^4$ (c and f), on a planet spinning at $\Omega = 2\Omega_\oplus$. The size of drops is fixed to $r_p = 10^{-3}$ m. The solid blue line with overlaid white dots to improve its visibility denotes $z_{\rm col}$, the black-and-white dashed line denotes the depth z_β, and the solid red line separates the impactors that are influenced by rotation in the aftermath of the impact (on the left-hand side) from those that are affected by rotation deeper in the mantle (on the right-hand side).

Results for a target planet spinning faster at $\Omega = 5\Omega_\oplus$ (figure 9) highlight that vortical columns form at lower depths when rotation is stronger; specifically here with $g = g_\oplus$, all the impactors we consider transition to a vortical column in the aftermath of the impact i.e. $z_{\rm col} = 0$. As a result the efficiency $\mathcal{E}_i(z)$ is lower than in figure 8 when the cloud reaches the depth $z = z_\beta$, hence the discrepancy between $\mathcal{E}_i(z)$ and $\mathcal{E}_i^{\rm th}(z)$ is exacerbated.

The efficiency of impactors verifying $z_{\rm col} > 0$ (on the right-hand side of the vertical red line in figure 8) reduces when Ω increases. However, clouds that verify $z_{\rm col} = 0$ are unaffected by any further increase of Ω, as illustrated in figure 10a. As long as Ω is sufficiently low (on the left-hand side of the vertical red line), a faster spinning reduces both $z_{\rm col}$ and z_β and thus the efficiency $\mathcal{E}_i(z_\beta)$. Conversely, when Ω is above the critical value Ω_c indicated by the vertical red line, impactors verify $z_{\rm col} = 0$ and we observe that the efficiency becomes independent of Ω. Indeed, the

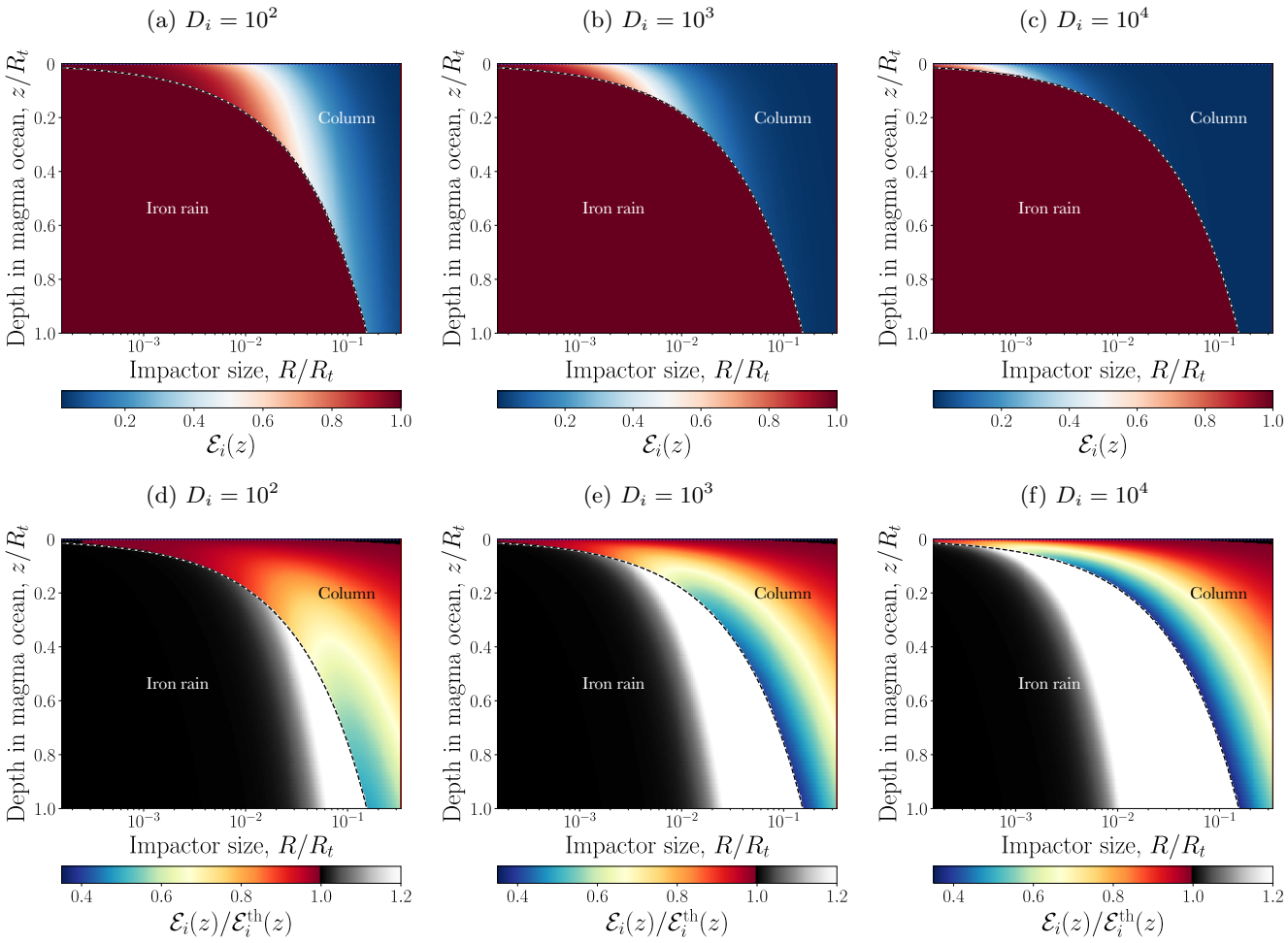

FIG. 9: Same as figure 8 but on a planet that is now spinning at $\Omega = 5\Omega_\oplus$.

efficiency of vortical columns only depends on the metal dilution (see equation (D5)) which becomes independent of Ω when $z_{\rm col} = 0$ (see equation (16)).

For a given impactor radius R, all angular velocities above the critical threshold Ω_c have an identical influence on the cloud evolution and on metal-silicate mixing. This critical threshold is measured for several values of the gravity g and shown in figure 10b as a function of the impactor radius up to $R/R_t = 1$. The increase of Ω_c with R when $R < 0.33R_t$ originates from larger impactors having more buoyancy and hence inertia. Thus, a larger angular velocity is required to guarantee that this inertia does not overcome the Coriolis force. Yet this intuitive result is not trivial since both $\dot{z}_f(z)$ and $r(z)$, which enter the definition of the Rossby number (7), increase with R/R_t. In the range $R/R_t \leq 0.33$, the ratio $\dot{z}_f(z)/r(z)$ increases with R/R_t, and hence the critical angular velocity Ω_c increases with R/R_t. Conversely, in the range $R/R_t \geq 0.33$, the critical angular velocity Ω_c is a decreasing function of R/R_t because of the decrease of $\dot{z}_f(z)/r(z)$ with increasing R/R_t.

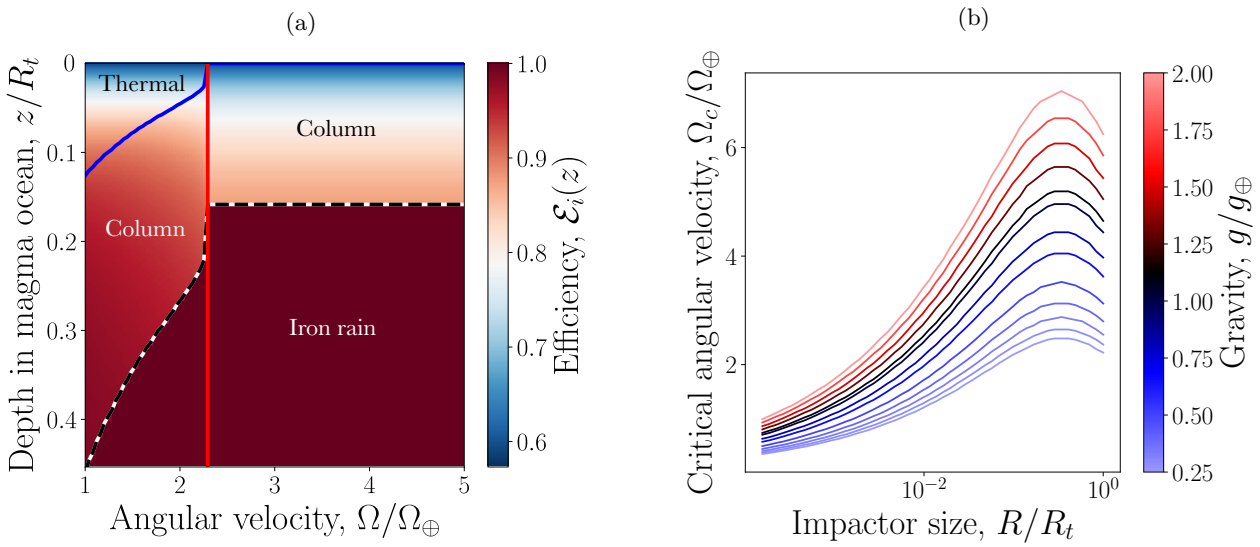

FIG. 10: (a) Influence of the angular velocity Ω on the transitions between dynamical regimes (from thermal to vortical column $z_{\rm col}$ (——), from vortical column to iron rain z_β (- - -), critical angular velocity Ω_c at which the thermal regime disappears and the flow is influenced by rotation in the aftermath of the impact (——)) and on the evolution of the efficiency $\mathcal{E}_i(z)$ with depth. The radius of the impactor is $R = 50$ km. (b) Evolution of the critical angular velocity Ω_c as a function of impactor size and for various values of g. For both figures, the size of the metal drops is $r_p = 10^{-3}$ m.

V. DISCUSSION AND CONCLUDING REMARKS

Accounting for planetary rotation reconciles the existing models of a turbulent thermal and an iron rain (see figure 4), which appeared to be in contradiction. Our results suggest that, after each impact, a turbulent thermal of metal and silicates sinks in the magma ocean, but transitions first to a swirling column strongly influenced by rotation, and then to a rain of iron drops. The transition from a thermal to a swirling column occurs at a critical depth $z_{\rm col}$, at which the inertia of the cloud equals the Coriolis force, meaning that the Rossby number Ro of equation (7) equals unity. In this regime, a vortical column grows by detrainment of metal drops from a drop-laden frontal sphere to a swirling wake. This regime ends when detrainment completes (figure 4). At depths larger than z_β, we predict that metal drops rain out from the column into an iron rain.

These effects of rotation on the dynamics of the cloud of metal drops have consequences on their chemical equilibration with silicates. At depths larger than $z_{\rm col}$ but smaller than z_β, the equilibration happens in a swirling column and is limited by the mass of silicates entrained in this column. Indeed the entrainment of ambient silicates is reduced in this regime compared to that in turbulent thermals. Thus, the regime of vortical columns is characterised by a reduced metal dilution $\Delta(z)$ compared to the dilution $\Delta_{\rm th}(z)$ of a reference turbulent thermal at the same depth (figure 6).

We therefore predict an equilibration efficiency that is lower than previous estimates that neglect planetary rotation. Conversely, at depth larger than z_β, during the regime of iron rain, metal drops interact with a continuously-renewed volume of silicates. Thanks to this renewal of silicates, chemical transfers are efficient and full equilibration is reached at a typical depth $z_\beta + l_{\rm eq}$ with $l_{\rm eq}$ the equilibration length scale, equal to 200 m for $D_i = 10^4$ (see paragraph IV B 1 c).

In the first two regimes of turbulent thermal and vortical column, metal equilibrates with a volume of silicates and hence dilution is the key parameter controlling the efficiency. The efficiency decreases with the impactor size in both regimes (figures 8a-8c and 9a-9c), and it increases with decreasing angular velocities Ω in the vortical regime (see figure 10a when $\Omega < \Omega_c$). In the regime of iron rain involving a continuously-renewed volume of silicates, the decisive quantity affecting mass transfers is the equilibration length scale $l_{\rm eq}$ (equation (18)).

These results show that the depth of the magma ocean, and more specifically its value relative to the three depths $z_{\rm col}$, z_β and $z_\beta + l_{\rm eq}$, controls the efficiency of chemical equilibration.

The above conclusions are based on strong assumptions. When metal drops rain out of the vortical column, they may partly entrain some contaminated silicates. This ability of particles to drag the interstitial fluid that separates them has been investigated in the literature; it depends on the interparticle distance and how it compares with a critical distance of hydrodynamical interaction (Harada et al. 2012, Yamamoto 2015) that is a function of the dynamics of the flow past the particles (Daniel et al. 2009, Guazzelli and Hinch 2011, Subramanian and Koch 2008). These effects lack understanding and have therefore been neglected in the present work. Additional experiments involving suspensions should control the interparticle distance, as well as the size and settling velocity of particles, examining various ratios of particle inertia to viscous dissipation, i.e. the particle Reynolds number. Such experiments would improve our ability to account for a partial drag of silicates by the iron drops. This effect would lead to a smoother evolution of the efficiency $\mathcal{E}_i(z)$ at depths $z > z_\beta$. In addition, we have neglected the flow caused by the difference in composition between the silicates in the vortical column and the surrounding magma ocean. This could lead to the vertical displacement of the column within the ocean. Finally, we have assumed that the convective motions in the magma ocean are much weaker than the flows in the thermal and vortical column. However, convective motions will certainly affect the long-term fate of the vortical column.

The present work focuses on the dynamical regimes and the equilibration of a cloud of metal drops falling parallel to the rotation axis of the target planet. This corresponds to a scenario of an impact near the poles. Investigation of the effect of rotation at different latitudes as in Maas et al. (2021) would be beneficial. The misalignment between

$\vec{g}$ and $\vec{\Omega}$ might affect the turbulent stirring of metal drops, and their dispersion and equilibration in the mantle. To tackle the misalignment between $\vec{g}$ and $\vec{\Omega}$, experiments could be performed using an off-centered tank on a rotating table and the centrifugal force to mimic inclined gravity. However, the range of accessible angles could be limited, so numerical simulations would be well-suited to investigate this. Simulations could also incorporate the heating during the impact. If the metal cloud is warmer, we expect that an upward buoyancy force of thermal origin will reduce the cloud inertia and therefore favour a transition to the columnar regime at a lower depth.

Additional experiments at faster rotation rates or starting with releases of lower buoyancy would be beneficial to model small impactors on a fast-spinning planet whose dynamics is constrained by planetary rotation at the top of the magma ocean ($z_{\rm col} = 0$). They could be complemented by new experiments investigating the role of planetary rotation during the phase of impact and crater collapse, and how dilution by entrainment of already rotating fluid plays any part in the cloud dynamics and onset of settling. Together, they could improve the modelling of the critical condition $\Omega \geq \Omega_c$ for the onset of vortical columns at the very surface of the planet. As regards the vortical regime, additional experiments at larger scale with larger initial cloud buoyancy or lower rotation rates would be beneficial to better constrain the process of detrainment and the subsequent raining out of metal drops, and how it may be influenced by Ekman pumping if the latter develops before raining out from the swirling motions.

VI. ACKNOWLEDGEMENTS

This work was supported by the Programme National de Planétologie (PNP) of CNRS-INSU co-funded by CNES.

Appendix A: Separation of released fluid and particles

Figure 11 shows that after some depth, particles rain out of the turbulent cloud, a process referred to as 'separation'. This separation has already been observed in the literature (Bush 2003, Deguen et al. 2011, Rahimipour and Wilkinson 1992). When a turbulent thermal develops, it initially accelerates and reaches a maximum velocity $\sim U_{\rm ref}$ that is larger than the individual settling velocity w_s of particles. Consequently, particles are forced to swirl inside the fast turbulent eddies. However, as the turbulent thermal grows in size, it decelerates. When its velocity eventually becomes lower than the settling velocity w_s, eddies are not vigorous enough to sustain the particles which rain out of the cloud. Separation happens when the cloud velocity approaches the individual settling velocity of particles i.e. $\dot{z}(z_{\rm sep}) \simeq w_s$ where $z_{\rm sep}$ is the depth of separation. After separation, particles fall as a *swarm*: the cloud vertical

velocity is constant and approximately equal to w_s, and the swarm keeps an approximately constant horizontal extent.

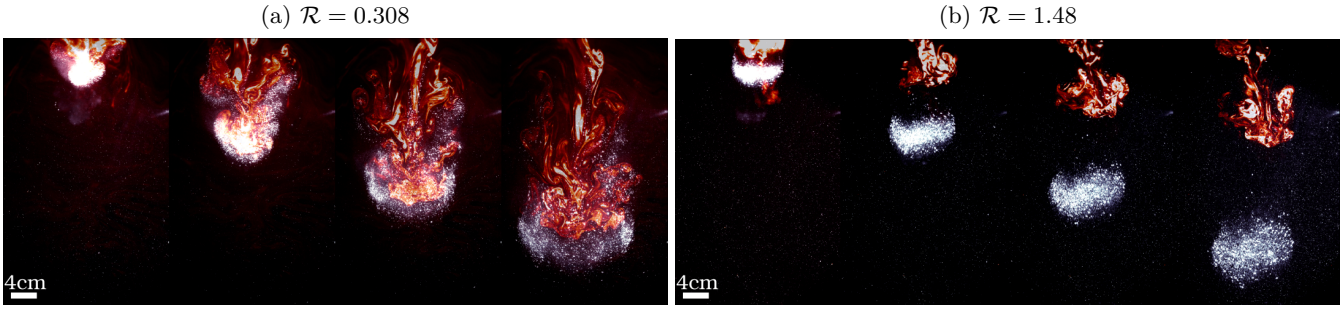

FIG. 11: Snapshots showing the gradual separation between particles (in white) and the released fresh water (in orange), all the faster as the Rouse number $\mathcal{R}$ increases from (a) to (b). Time intervals Δt between snapshots are (a) $\Delta t = 3.0s$ and (b) $\Delta t = 1.2s$.

To predict separation, we use a *local* Rouse number $\mathcal{R}^*(z)$ that compares the settling velocity w_s of a particle with the *local* cloud velocity $\dot{z}(z)$ at depth z, i.e.

$$\mathcal{R}^*(z) = \frac{w_s}{\dot{z}(z)}. \tag{A1}$$

When $\mathcal{R}^*(z) < 1$, eddies are vigorous enough to sustain particles so the cloud behaves as a thermal. Conversely, when $\mathcal{R}^*(z) > 1$, particles fall as a swarm. Our own experimental measurements (Kriaa et al. 2022) as well as past studies (Deguen et al. 2011, Wang 2014) validated this separation criterion. Even if the velocity $\dot{z}(z)$ decreases during the thermal regime, the threshold $\mathcal{R}^*(z) = 1$ is never reached in the planetary regimes that we explore, hence the swarm regime is not considered in the main text.

In equation (A1), the velocity $\dot{z}(z)$ is estimated following the model of Escudier and Maxworthy (1973) for a turbulent thermal in which buoyancy is the sole volume force. Neglecting added mass as suggested by Bush (2003), Deguen et al. (2011), we obtain

$$\dot{z}(z) = \sqrt{\frac{gD_{\rm cyl}}{2\alpha}\left(\frac{\rho_0}{\rho_f} - 1\right)} \times \frac{\sqrt{\frac{1}{2}((1+\alpha\overline{z})^4 - 1) + \frac{\alpha\overline{z}}{2}(\frac{\rho_0}{\rho_f} - 1)}}{(1+\alpha\overline{z})^3 + \frac{\rho_0}{\rho_f} - 1}, \tag{A2}$$

where $\overline{z} = 2z/D_{\rm cyl}$.

Appendix B: Results for a detrainment coefficient $\beta = 0.05$

Figure 12 shows the evolution of the equilibration efficiency for several impactor sizes when $\beta = 0.05$ and $\Omega = 2\Omega_\oplus$, and figure 13 shows the same results when $\Omega = 5\Omega_\oplus$. Vortical columns dilute less than turbulent thermals (see section IV C), and the lower β, the deeper the maximum depth of detrainment z_β (equation (11)). As a result, the lower β the larger the discrepancy between the equilibration efficiency of a vortical column and that of a turbulent thermal, down to a ratio $\mathcal{E}_i/\mathcal{E}_i^{\rm th} \simeq 0.1$ for $D_i = 10^4$ and $\Omega = 5\Omega_\oplus$ (see figure 13f).

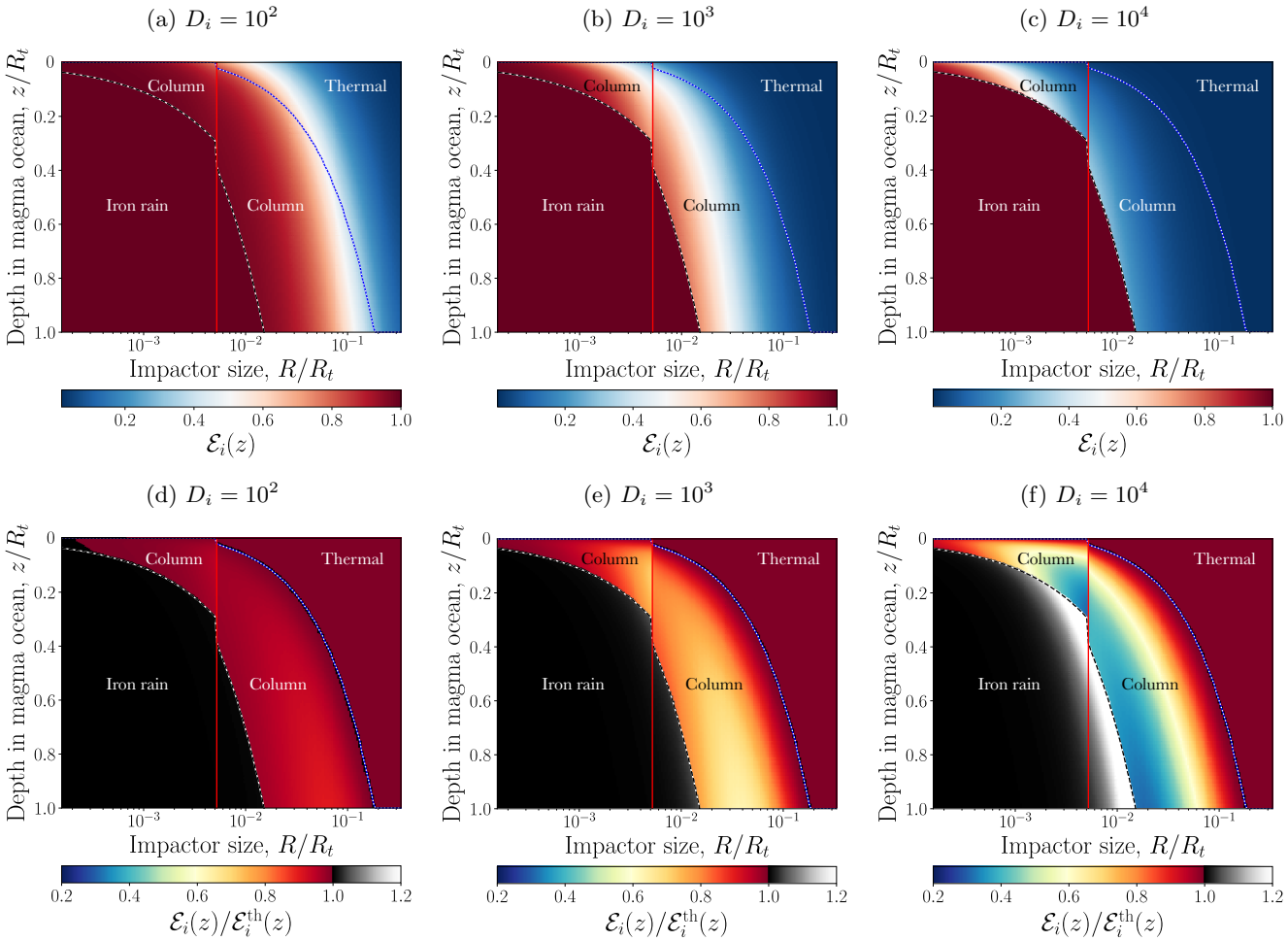

FIG. 12: Same as figure 8 for $\beta = 0.05$. Equilibration efficiency $\mathcal{E}_i$ (a-c) and ratio $\mathcal{E}_i/\mathcal{E}_i^{\rm th}$ (d-f) as a function of impactor size and magma ocean depth for partition coefficients $D_i = 10^2$ (a and d), $D_i = 10^3$ (b and e) and $D_i = 10^4$ (c and f), on a planet spinning at $\Omega = 2\Omega_\oplus$. See figure 8 for more information.

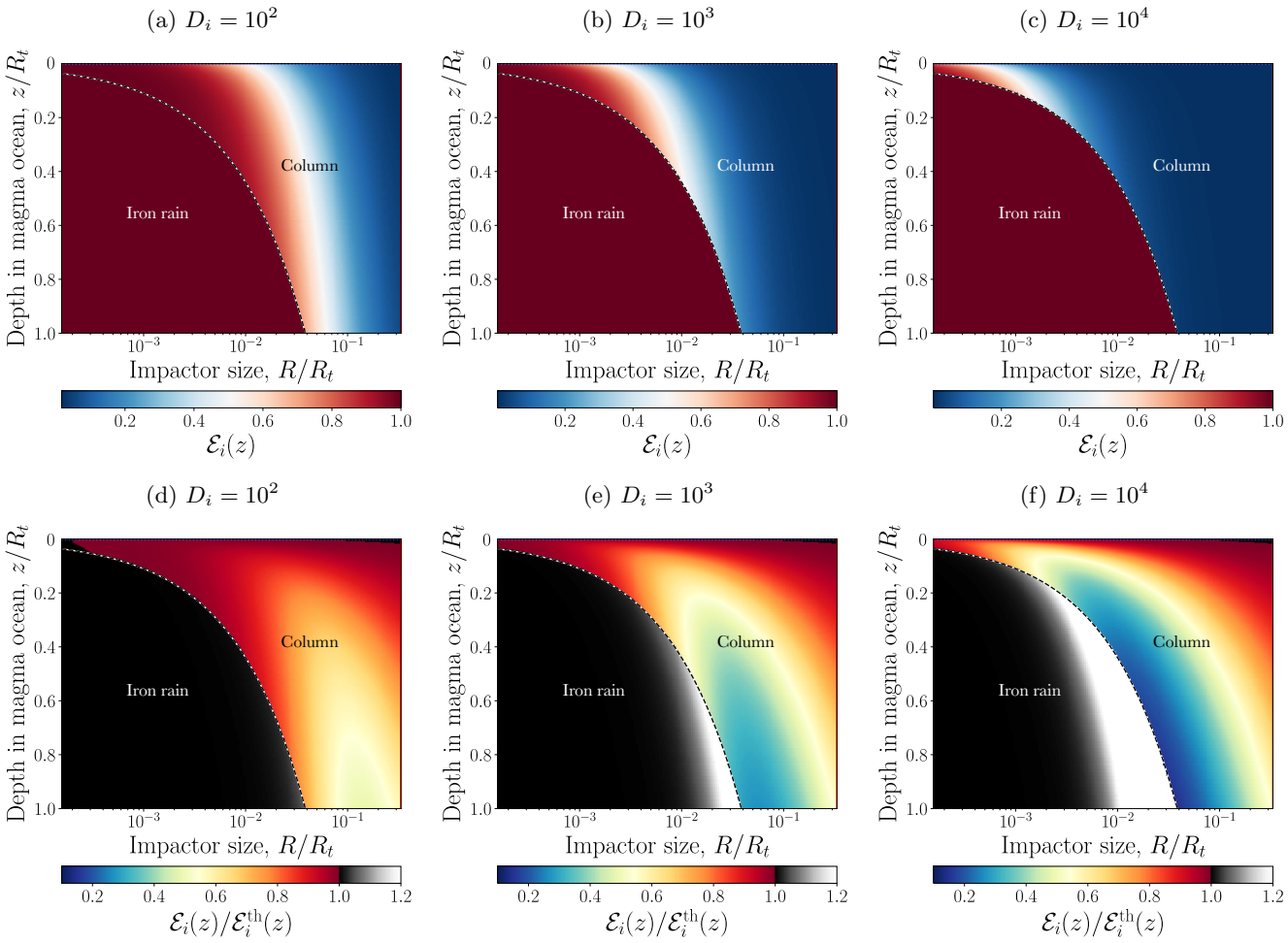

FIG. 13: Same as figure 12 but on a planet that is now spinning at $\Omega = 5\Omega_\oplus$.

Appendix C: thermodynamic equilibrium and uniformity in the flow

As stated in section IV B 1, the efficiency quantifies mass transfers under the assumptions that a thermodynamic equilibrium is reached by metal and silicates during the cloud fall, and that the cloud is uniform in concentration.

The first requirement translates as a condition $\tau_\chi \ll 2r/\dot{z}$ where τ_χ is the timescale of chemical transfers and $2r/\dot{z}$ is the advective timescale i.e. the typical timescale for the variation of the macroscopic cloud properties (such as its density and radius): this condition means that chemical transfers should complete long before the cloud properties vary to ensure a thermodynamic equilibrium is reached at any depth of the cloud fall. The timescale τ_χ is provided by Deguen et al. (2014) in their equation (22)

$$\tau_\chi \propto \frac{(2r)^2}{\kappa_s} Sc^{-1/2} Re^{-1/2} We^{-3/5}. \tag{C1}$$

$We = \rho_m 2r\dot{z}^2/\sigma$ is the Weber number with σ the iron-silicate interfacial tension, Sc is the Schmidt number that is the ratio of kinematic viscosity and diffusivity in silicates, and $Re = 2r\dot{z}/\nu_m$ – see table II for notations and Deguen et al. (2014) for more information. We verify that the requirement $\tau_\chi \ll 2r/\dot{z}$ is met for all scenarios explored in figure 5a almost immediately (for the impactors that are influenced by rotation immediately in the aftermath of the impact, we find $2r/\dot{z}\tau_\chi > 1$ as soon as $z \geq 0.9$ km i.e. $z/z_\beta \geq 2 \times 10^{-3}$; for the other impactors, we find $2r/\dot{z}\tau_\chi > 1$ as soon as $z/z_{\text{col}} \geq 5 \times 10^{-3}$).

The second requirement translates as a condition $\tau_K \ll \tau_\chi$ with τ_K a timescale of dissipation of heterogeneities within the cloud. This condition means that as chemical transfers proceed forward, heterogeneities are smoothed out by turbulence much faster, so that the cloud can be considered homogeneous during mass transfers. While the literature contains evidences of heterogeneities within turbulent thermals (Lherm 2021), past studies in a variety of contexts have proved the robustness and accuracy of predictions based on the assumption of homogeneity within the turbulent thermal (Ayotte and Fernando 1994, Deguen et al. 2014, Fernando 1998, Helfrich 1994, Landeau et al. 2021, Morton et al. 1956, Turner 1986) and in particle clouds (Deguen et al. 2011, Kriaa et al. 2022, Landeau et al. 2014). This can be verified by computing the timescale of homogenisation based on local velocity gradients. Deguen et al. (2014) have shown that the turbulence that develops inside turbulent thermals can be modelled as a homogeneous isotropic turbulence at first order. Hence the timescale of local homogenisation is the Kolmogorov timescale based on the cloud radius and entrainment velocity

$$\tau_K = \sqrt{\frac{\nu r}{\alpha^3 \dot{z}^3}}, \tag{C2}$$

which does verify the condition $\tau_K \ll \tau_\chi$ for all impactors and all depths in the general configuration of figure 5a ($\beta = 0.12$, $\Omega = 2\Omega_\oplus$, $g = g_\oplus$, $r_p = 10^{-3}$ m).

As regards the vortical regime, renewal of the metal volume fraction $\phi(z)$ within the frontal sphere happens on a timescale τ_β. We assume that turbulence is little altered in the frontal sphere whose Reynolds number remains constant, consequently the timescale of homogenisation τ_K is unaltered, and so is the timescale of chemical transfers τ_χ. Then, we verify that the condition $\tau_K \ll \tau_\chi$ is verified for all impactors at all depths. As for the condition $\tau_\chi \ll \tau_\beta$, it is verified by all vortical columns of figure 5a having $z_{\text{col}} > 0$. For the other clouds in the range $R/R_t \leq 4.99 \times 10^{-3}$, in the worst case we find $\tau_\beta/\tau_\chi > 1$ as soon as $z/z_\beta \geq 1 \times 10^{-4}$.

Finally, consider the regime of iron rain with iron drops raining out of the vortical column. In this regime homogeneity is guaranteed: indeed, as a first approximation, metal drops fall individually and cross quiescent unpolluted

fluid whose concentration all around each drop is still the initial silicate concentration of the magma ocean c_s^0. However, a thermodynamic equilibrium can only be reached after the drops have travelled a distance long enough to have completed mass transfers with the ambient, thus reaching the ideal equilibrium described by $\mathcal{M}_{\rm i,max}$. We show in appendix E how to quantify a transient mixing efficiency before this ultimate thermodynamic equilibrium is reached.

Appendix D: Equilibration efficiency of a uniform mixture of metal and silicates

To quantify the mass transfer of an element i between metal and silicates, consider some mass of metal $m_m(z)$ and some mass of silicates $m_s(z)$ that are sufficiently uniformly mixed to be at thermodynamic equilibrium at a given depth z (right-hand side of equation (D1)), and the initial state of both masses when metal is isolated with a concentration c_m^0, and when silicates are isolated with a concentration c_s^0 (left-hand side of equation (D1)). Mass conservation between these two states reads

$$m_m(z)c_m^0 + m_s(z)c_s^0 = m_m(z)c_m^{\rm eq}(z) + m_s(z)c_s^{\rm eq}(z). \tag{D1}$$

In equation (D1), the masses $m_m(z)$ and $m_s(z)$ are those involved in chemical transfers when either a turbulent thermal or a vortical column (i.e. the combination of a frontal sphere and its wake) is at depth z. The mass concentration $c_m^{\rm eq}(z)$ (respectively $c_s^{\rm eq}(z)$) is the concentration of i in the metal (respectively in silicates) when thermodynamic equilibrium is reached. The condition of thermodynamic equilibrium imposes that $c_s^{\rm eq}(z) = c_m^{\rm eq}(z)/D_i$. Using this constraint of equilibrium in equation (D1) and isolating the equilibrium concentration of metal $c_m^{\rm eq}(z)$ yields

$$c_m^{\rm eq}(z) = \frac{m_m(z)c_m^0 + m_s(z)c_s^0}{m_m(z) + m_s(z)/D_i} \tag{D2}$$

The equilibration efficiency quantifies the net mass transfer of element from the very initial state (at impact) to the state of equilibrium $c_m^{\rm eq}(z)$ so that

$$\mathcal{E}_i(z) = \frac{m_m(z)|c_m^{\rm eq}(z) - c_m^0|}{\mathcal{M}_{\rm i,max}}, \tag{D3}$$

with $\mathcal{M}_{\mathrm{i,max}} = m_0|c_m^0 - D_i c_s^0|$. By subtracting c_m^0 from both sides in equation (D2), and using equation (D3), we readily obtain

$$\mathcal{E}_i(z) = \frac{m_m(z)m_s(z)}{m_0}\frac{1}{m_s(z) + D_i m_m(z)}. \tag{D4}$$

This last equation can be rearranged to take the exact same form as the efficiency of a turbulent thermal expressed by Deguen et al. (2014),

$$\mathcal{E}_i(z) = \frac{k(z)}{1 + \frac{D_i}{\Delta(z)}}, \tag{D5}$$

with $k(z) = m_m(z)/m_0$ and $\Delta(z) = m_s(z)/m_m(z)$ is the metal dilution. Importantly, equation (D5) is valid for any uniform structure containing a mass $m_m(z)$ of metal and a mass $m_s(z)$ of silicates. Therefore, it applies for turbulent thermals with $\Delta(z) = \Delta_{\mathrm{th}}(z)$ and the equation (13) is recovered. It also applies for a vortical column with $\Delta(z) = \Delta_{\mathrm{col}}(z)$ and the equation (15) is recovered.

Appendix E: Equilibration efficiency for a swarm in the regime of iron rain

Mass transfers in the regime of iron rain are characterised by an exponential evolution of the concentration in element i in depth, on a characteristic length scale l_{eq} provided in equation (18) (see Lherm and Deguen 2018). The mass concentration $c_m(z)$ in element i in the metal phase varies to reach the equilibrium concentration $D_i c_s^0$ and verifies

$$c_m(z) - D_i c_s^0 = [c_m(z_\beta) - D_i c_s^0] \exp\left(-\frac{z - z_\beta}{l_{\mathrm{eq}}}\right), \tag{E1}$$

which applies for $z \geq z_\beta$. Then it follows that

$$\frac{m_0[c_m(z) - c_m^0]}{\mathcal{M}_{\mathrm{i,max}}} = \frac{m_0}{\mathcal{M}_{\mathrm{i,max}}}[D_i c_s^0 - c_m^0] + \frac{m_0}{\mathcal{M}_{\mathrm{i,max}}}[c_m(z) - D_i c_s^0] \tag{E2}$$

$$= \frac{m_0}{\mathcal{M}_{\mathrm{i,max}}}[D_i c_s^0 - c_m^0] + \frac{m_0}{\mathcal{M}_{\mathrm{i,max}}}[c_m(z_\beta) - D_i c_s^0] \exp\left(-\frac{z - z_\beta}{l_{\mathrm{eq}}}\right)$$

$$= \frac{m_0}{\mathcal{M}_{\mathrm{i,max}}}[D_i c_s^0 - c_m^0]\left[1 - \exp\left(-\frac{z - z_\beta}{l_{\mathrm{eq}}}\right)\right] + \tag{E3}$$

$$\frac{m_0}{\mathcal{M}_{\mathrm{i,max}}}[c_m(z_\beta) - c_m^0] \exp\left(-\frac{z - z_\beta}{l_{\mathrm{eq}}}\right)$$

From the definitions of $\mathcal{M}_{\mathrm{i,max}}$ and of the equilibration efficiency in equation (17), the latter finally reads

$$\mathcal{E}_i(z) = 1 + [\mathcal{E}_i(z_\beta) - 1] \exp\left(-\frac{z - z_\beta}{l_{\mathrm{eq}}}\right). \tag{E4}$$

Under the present form, equation (E4) applies for clouds that transition from the regime of vortical column to the iron rain regime, but it can be generalised to other contexts, should the swarm regime be taken into account[1].

DATA AVAILABILITY

The data underlying this article will be shared on reasonable request to the corresponding author.

DECLARATION OF INTERESTS

The authors declare that they have no known competing financial interests or personal relationships that could have appeared to influence the work reported in this paper.

Abe, Y. and Matsui, T. (1985), 'The formation of an impact-generated H2O atmosphere and its implications for the early thermal history of the Earth', *Journal of Geophysical Research: Solid Earth* **90**(S02), C545–C559.

Ayotte, B. A. and Fernando, H. J. S. (1994), 'The Motion of a Turbulent Thermal in the Presence of Background Rotation', *Journal of the Atmospheric Sciences* **51**(13), 1989–1994.

[1] The position z_β can be replaced with $z = 0$ for a cloud behaving as a swarm immediately after impact, and it can be replaced with the depth of separation where $\mathcal{R}^*(z) = 1$ for a cloud transitioning from the thermal regime to the swarm regime without ever behaving as a vortical column.

Badro, J., Aubert, J., Hirose, K., Nomura, R., Blanchard, I., Borensztajn, S. and Siebert, J. (2018), 'Magnesium Partitioning Between Earth's Mantle and Core and its Potential to Drive an Early Exsolution Geodynamo', *Geophysical Research Letters* **45**(24), 13,240–13,248.

Baines, P. G. (2001), 'Mixing in flows down gentle slopes into stratified environments', *Journal of Fluid Mechanics* **443**, 237–270.

Bercovici, D. and Ricard, Y. (2014), 'Plate tectonics, damage and inheritance', *Nature* **508**(7497), 513–516.

Bush, J. W. M. (2003), 'Particle clouds in homogeneous and stratified environments', *JFM* **489**, 23–54.

Bush, J. W. M., Stone, H. A. and Bloxham, J. (1995), 'Axial drop motion in rotating fluids', *Journal of Fluid Mechanics* **282**, 247–278.

Canup, R. M. (2012), 'Forming a Moon with an Earth-like Composition via a Giant Impact', *Science* **338**(6110), 1052–1055.

Canup, R. M. and Asphaug, E. (2001), 'Origin of the Moon in a giant impact near the end of the Earth's formation', *Nature* **412**(6848), 708–712.

Carlotti, P. and Hunt, G. R. (2017), 'An entrainment model for lazy turbulent plumes', *Journal of Fluid Mechanics* **811**, 682–700.

Chambers, J. E. (2004), 'Planetary accretion in the inner Solar System', *Earth and Planetary Science Letters* **223**(3), 241–252.

Ćuk, M. and Stewart, S. T. (2012), 'Making the Moon from a Fast-Spinning Earth: A Giant Impact Followed by Resonant Despinning', *Science* **338**(6110), 1047–1052.

Daher, H., Arbic, B. K., Williams, J. G., Ansong, J. K., Boggs, D. H., Müller, M., Schindelegger, M., Austermann, J., Cornuelle, B. D., Crawford, E. B., Fringer, O. B., Lau, H. C. P., Lock, S. J., Maloof, A. C., Menemenlis, D., Mitrovica, J. X., Green, J. A. M. and Huber, M. (2021), 'Long-Term Earth-Moon Evolution With High-Level Orbit and Ocean Tide Models', *Journal of Geophysical Research: Planets* **126**(12), e2021JE006875.

Dahl, T. W. and Stevenson, D. J. (2010), 'Turbulent mixing of metal and silicate during planet accretion — And interpretation of the Hf–W chronometer', *Earth and Planetary Science Letters* **295**(1), 177–186.

Daniel, W. B., Ecke, R. E., Subramanian, G. and Koch, D. L. (2009), 'Clusters of sedimenting high-Reynolds-number particles', *Journal of Fluid Mechanics* **625**, 371–385.

Davidson, P. A., Staplehurst, P. J. and Dalziel, S. B. (2006), 'On the evolution of eddies in a rapidly rotating system', *Journal of Fluid Mechanics* **557**, 135–144.

de Leeuw, J., Lamb, M. P., Parker, G., Moodie, A. J., Haught, D., Venditti, J. G. and Nittrouer, J. A. (2020), 'Entrainment and suspension of sand and gravel', *Earth Surface Dynamics* **8**(2), 485–504.

de Rooy, W. C., Bechtold, P., Fröhlich, K., Hohenegger, C., Jonker, H., Mironov, D., Pier Siebesma, A., Teixeira, J. and Yano, J.-I. (2013), 'Entrainment and detrainment in cumulus convection: An overview', *Quarterly Journal of the Royal Meteorological Society* **139**(670), 1–19.

de Rooy, W. C. and Siebesma, A. P. (2008), 'A Simple Parameterization for Detrainment in Shallow Cumulus', *Monthly Weather Review* **136**(2), 560–576.

Deguen, R., Landeau, M. and Olson, P. (2014), 'Turbulent metal–silicate mixing, fragmentation, and equilibration in magma oceans', *Earth and Planetary Science Letters* **391**, 274–287.

Deguen, R., Olson, P. and Cardin, P. (2011), 'Experiments on turbulent metal-silicate mixing in a magma ocean', *Earth and Planetary Science Letters* **310**(3), 303–313.

Dodds, K. H., Bryson, J. F. J., Neufeld, J. A. and Harrison, R. J. (2021), 'The Thermal Evolution of Planetesimals During Accretion and Differentiation: Consequences for Dynamo Generation by Thermally-Driven Convection', *Journal of Geophysical Research: Planets* **126**(3), e2020JE006704.

Escudier, M. P. and Maxworthy, T. (1973), 'On the motion of turbulent thermals', *Journal of Fluid Mechanics* **61**(3), 541–552.

Fernando, HJS. (1998), 'Development of a point plume in the presence of background rotation', *Physics of Fluids* **10**(2369).

Fischer, R. A., Nakajima, Y., Campbell, A. J., Frost, D. J., Harries, D., Langenhorst, F., Miyajima, N., Pollok, K. and Rubie, D. C. (2015), 'High pressure metal–silicate partitioning of Ni, Co, V, Cr, Si, and O', *Geochimica et Cosmochimica Acta* **167**, 177–194.

Greenspan, H. P. (1968), The theory of rotating fluids, Technical report, Massachusetts Inst of Tech Cambridge Dept of Mathematics.

Guazzelli, É. and Hinch, J. (2011), 'Fluctuations and Instability in Sedimentation', *Annual Review of Fluid Mechanics* **43**(1), 97–116.

Harada, S., Mitsui, T. and Sato, K. (2012), 'Particle-like and fluid-like settling of a stratified suspension', *The European Physical Journal E* **35**(1), 1.

Helfrich, K. R. (1994), 'Thermals with background rotation and stratification', *Journal of Fluid Mechanics* **259**, 265–280.

Ichikawa, H., Labrosse, S. and Kurita, K. (2010), 'Direct numerical simulation of an iron rain in the magma ocean', *Journal of Geophysical Research: Solid Earth* **115**(B1).

Jennings, E. S., Jacobson, S. A., Rubie, D. C., Nakajima, Y., Vogel, A. K., Rose-Weston, L. A. and Frost, D. J. (2021), 'Metal–silicate partitioning of W and Mo and the role of carbon in controlling their abundances in the bulk silicate earth', *Geochimica et Cosmochimica Acta* **293**, 40–69.

Karki, B. B. and Stixrude, L. P. (2010), 'Viscosity of MgSiO3 liquid at Earth's mantle conditions: Implications for an early magma ocean', *Science (New York, N.Y.)* **328**(5979), 740–742.

Kleine, T., Münker, C., Mezger, K. and Palme, H. (2002), 'Rapid accretion and early core formation on asteroids and the terrestrial planets from Hf-W chronometry', *Nature* **418**(6901), 952–955.

Kono, M. (2010), 5.01 - Geomagnetism: An Introduction and Overview, *in* 'Treatise on Geophysics (First Edition)', Vol. 5.

Kriaa, Q., Subra, E., Favier, B. and Le Bars, M. (2022), 'Effects of particle size and background rotation on the settling of particle clouds', *Physical Review Fluids* **7**(12), 124302.

Labrosse, S. (2015), 'Thermal evolution of the core with a high thermal conductivity', *Physics of the Earth and Planetary Interiors* **247**, 36–55.

Lai, A. C. H., Wang, R.-Q., Law, A. W.-K. and Adams, E. E. (2016), 'Modeling and experiments of polydisperse particle clouds', *Environmental Fluid Mechanics* **16**(4), 875–898.

Landeau, M., Deguen, R. and Olson, P. (2014), 'Experiments on the fragmentation of a buoyant liquid volume in another liquid', *Journal of Fluid Mechanics* **749**, 478–518.

Landeau, M., Deguen, R., Phillips, D., Neufeld, J. A., Lherm, V. and Dalziel, S. B. (2021), 'Metal-silicate mixing by large Earth-forming impacts', *Earth and Planetary Science Letters* **564**, 116888.

Lherm, V. (2021), Thermal and chemical partitioning dynamics during the differentiation of terrestrial planets, PhD thesis, Université de Lyon.

Lherm, V. and Deguen, R. (2018), 'Small-Scale Metal/Silicate Equilibration During Core Formation: The Influence of Stretching Enhanced Diffusion on Mixing', *Journal of Geophysical Research: Solid Earth* **123**(12), 10,496–10,516.

Lherm, V., Deguen, R., Alboussière, T. and Landeau, M. (2022), 'Rayleigh–Taylor instability in impact cratering experiments', *Journal of Fluid Mechanics* **937**, A20.

Maas, C., Manske, L., Wünnemann, K. and Hansen, U. (2021), 'On the fate of impact-delivered metal in a terrestrial magma ocean', *Earth and Planetary Science Letters* **554**, 116680.

Maxworthy, T. (1970), 'The flow created by a sphere moving along the axis of a rotating, slightly-viscous fluid', *Journal of Fluid Mechanics* **40**(3), 453–479.

Minkov, E., Ungarish, M. and Israeli, M. (2002), 'The motion generated by a rising particle in a rotating fluid – numerical solutions. Part 2. The long container case', *Journal of Fluid Mechanics* **454**, 345–364.

Moore, D. W., Saffman, P. G. and Stewartson, K. (1969), 'The structure of free vertical shear layers in a rotating fluid and the motion produced by a slowly rising body', *Philosophical Transactions of the Royal Society of London. Series A, Mathematical and Physical Sciences* **264**(1156), 597–634.

Morton, B. R., Taylor, G. I. and Turner, J. S. (1956), 'Turbulent gravitational convection from maintained and instantaneous sources', *Proceedings of the Royal Society of London. Series A. Mathematical and Physical Sciences* **234**(1196), 1–23.

Nakajima, M., Golabek, G. J., Wünnemann, K., Rubie, D. C., Burger, C., Melosh, H. J., Jacobson, S. A., Manske, L. and Hull, S. D. (2021), 'Scaling laws for the geometry of an impact-induced magma ocean', *Earth and Planetary Science Letters* **568**, 116983.

Olson, P. (2015), 8.01 - Core Dynamics: An Introduction and Overview, *in* G. Schubert, ed., 'Treatise on Geophysics (Second Edition)', Elsevier, Oxford, pp. 1–25.

Patterson, C., Tilton, G. and Inghram, M. (1955), 'Age of the Earth', *Science* **121**(3134), 69–75.

Qaddah, B., Monteux, J., Clesi, V., Bouhifd, M. A. and Le Bars, M. (2019), 'Dynamics and stability of an iron drop falling in a magma ocean', *Physics of the Earth and Planetary Interiors* **289**, 75–89.

Rahimipour, H. and Wilkinson, D. (1992), Dynamic behaviour of particle clouds, *in* '11th Australasian Fluid Mechanics Conference University of Tasmania, Hobart, Australia'.

Righter, K. (2011), 'Prediction of metal–silicate partition coefficients for siderophile elements: An update and assessment of PT conditions for metal–silicate equilibrium during accretion of the Earth', *Earth and Planetary Science Letters* **304**(1), 158–167.

Righter, K., Pando, K., Humayun, M., Waeselmann, N., Yang, S., Boujibar, A. and Danielson, L. R. (2018), 'Effect of silicon on activity coefficients of siderophile elements (Au, Pd, Pt, P, Ga, Cu, Zn, and Pb) in liquid Fe: Roles of core formation, late sulfide matte, and late veneer in shaping terrestrial mantle geochemistry', *Geochimica et Cosmochimica Acta* **232**, 101–123.

Rubie, D. C., Melosh, H. J., Reid, J. E., Liebske, C. and Righter, K. (2003), 'Mechanisms of metal–silicate equilibration in the terrestrial magma ocean', *Earth and Planetary Science Letters* **205**(3), 239–255.

Rudge, J. F., Kleine, T. and Bourdon, B. (2010), 'Broad bounds on Earth's accretion and core formation constrained by geochemical models', *Nature Geoscience* **3**(6), 439–443.

Samuel, H. (2012), 'A re-evaluation of metal diapir breakup and equilibration in terrestrial magma oceans', *Earth and Planetary Science Letters* **313–314**, 105–114.

Siebert, J., Badro, J., Antonangeli, D. and Ryerson, F. J. (2012), 'Metal–silicate partitioning of Ni and Co in a deep magma ocean', *Earth and Planetary Science Letters* **321–322**, 189–197.

Stewartson, K. (1952), 'On the slow motion of a sphere along the axis of a rotating fluid', *Mathematical Proceedings of the Cambridge Philosophical Society* **48**(1), 168–177.

Subramanian, G. and Koch, D. L. (2008), 'Evolution of clusters of sedimenting low-Reynolds-number particles with Oseen interactions', *Journal of Fluid Mechanics* **603**, 63–100.

Taylor, G. I. (1922), 'The motion of a sphere in a rotating liquid', *Proceedings of the Royal Society of London. Series A, Containing Papers of a Mathematical and Physical Character* **102**(715), 180–189.

Taylor, G. R. and Baker, M. B. (1991), 'Entrainment and detrainment in cumulus clouds', *Journal of the Atmospheric Sciences* **48**(1), 112–121.

Tonks, W. B. and Melosh, H. J. (1992), 'Core formation by giant impacts', *Icarus* **100**(2), 326–346.

Tonks, W. B. and Melosh, H. J. (1993), 'Magma ocean formation due to giant impacts', *Journal of Geophysical Research: Planets* **98**(E3), 5319–5333.

Touma, J. and Wisdom, J. (1994), 'Evolution of the Earth-Moon system', *The Astronomical Journal* **108**, 1943.

Turner, J. S. (1986), 'Turbulent entrainment: The development of the entrainment assumption, and its application to geophysical flows', *Journal of Fluid Mechanics* **173**, 431–471.

Ulvrová, M., Coltice, N., Ricard, Y., Labrosse, S., Dubuffet, F., Velímský, J. and Šrámek, O. (2011), 'Compositional and thermal equilibration of particles, drops, and diapirs in geophysical flows', *Geochemistry, Geophysics, Geosystems* **12**(10).

van Reeuwijk, M. and Craske, J. (2015), 'Energy-consistent entrainment relations for jets and plumes', *Journal of Fluid Mechanics* **782**, 333–355.

Vedensky, D. and Ungarish, M. (1994), 'The motion generated by a slowly rising disk in an unbounded rotating fluid for arbitrary Taylor number', *Journal of Fluid Mechanics* **262**, 1–26.

Wacheul, J.-B. and Le Bars, M. (2018), 'Experiments on fragmentation and thermo-chemical exchanges during planetary core formation', *Physics of the Earth and Planetary Interiors* **276**, 134–144.

Wang, H. and Law, A. W.-K. (2002), 'Second-order integral model for a round turbulent buoyant jet', *Journal of Fluid Mechanics* **459**, 397–428.

Wang, R.-Q. (2014), 'Large-Eddy Simulation (LES) of settling particle cloud dynamics', *International Journal of Multiphase Flow* **67**, 65–75.

Yamamoto, Y. (2015), 'Numerical simulation of concentration interface in stratified suspension: Continuum–particle transition', *International Journal of Multiphase Flow* **73**, 71–79.